JOURNAL OF GEOPHYSICAL RESEARCH, VOL. 113, B01302, doi:10.1029/2007JB005082, 2008

Earthquake nucleation on rate and state faults – Aging and slip laws

Jean-Paul Ampuero[1] and Allan M. Rubin[2]

Received 30 March 2007; revised 21 August 2007; accepted 10 October 2007; published 10 January 2008.

[1] We compare 2-D, quasi-static earthquake nucleation on rate-and-state faults under both "aging" and "slip" versions of the state evolution law. For both versions mature nucleation zones exhibit 2 primary regimes of growth: Well above and slightly above steady state, corresponding respectively to larger and smaller fault weakening rates. Well above steady state, aging-law nucleation takes the form of accelerating slip on a patch of fixed length. This length is proportional to b^{-1} and independent of a, where a and b are the constitutive parameters relating changes in slip speed and state to frictional strength. Under the slip law the nucleation zone is smaller and continually shrinks as slip accelerates. The nucleation zone is guaranteed to remain well above steady state only for values of a/b that are low by laboratory standards. Near steady state, for both laws the nucleation zone expands. The propagating front remains well above steady state, giving rise to a simple expression for its effective fracture energy G_c. This fracture energy controls the propagation style. For the aging law G_c increases approximately as the square of the logarithm of the velocity jump. This causes the nucleation zone to undergo quasi-static crack-like expansion, to a size asymptotically proportional to $b/(b-a)^2$. For the slip law G_c increases only as the logarithm of the velocity jump, and crack-like expansion is not an option. Instead, the nucleation zone grows as an accelerating unidirectional slip pulse. Under both laws the nucleation front propagates at a velocity larger than the slip speed by roughly $\mu'/b\sigma$ divided by the logarithm of the velocity jump, where μ' is the effective elastic shear modulus. For this prediction to be consistent with observed propagation speeds of slow slip events in subduction zones appears to require effective normal stresses as low as 1 MPa.

Citation: Ampuero, J.-P., and A. M. Rubin (2008), Earthquake nucleation on rate and state faults – Aging and slip laws, *J. Geophys. Res.*, *113*, B01302, doi:10.1029/2007JB005082.

1. Rate-and-State Background

[2] Although the modern rate- and state-dependent friction equations have been in use for over 2 decades, their implications for earthquake nucleation on deformable faults remain unclear. In their simplest and most common form, the frictional strength τ is written as

$$\tau = \sigma\left[f^* + a\ln\frac{V}{V^*} + b\ln\frac{V^*\theta}{D_c}\right], \tag{1}$$

where σ is the effective normal stress, here assumed constant, and f^* and V^* are reference values of the friction coefficient and sliding velocity (for a notation list see Table 1). The rate-dependent part of the strength, proportional to the logarithm of the sliding velocity V and the constitutive parameter a, is thought to reflect a thermally activated Arrhenius process involving the breaking of atomic bonds at contact points bridging the sliding surface [*Rice et al.*, 2001]. The state-dependent part of the strength, proportional to the logarithm of the state variable θ and the parameter b, is more mysterious, "state" being more difficult to observe than sliding velocity, but θ is thought to reflect the product of the true contact area and the intrinsic strength of those contacts.

[3] Two empirical equations for the evolution of θ, first formalized by *Ruina* [1983], are in common use. These are

$$\dot{\theta} = 1 - \frac{V\theta}{D_c} \qquad \text{(Aging law)}; \tag{2}$$

$$\dot{\theta} = -\frac{V\theta}{D_c}\ln\frac{V\theta}{D_c} \qquad \text{(Slip law)}; \tag{3}$$

where D_c is a characteristic slip distance. We refer to the first as the "aging law" because at zero slip speed θ increases as elaspsed time. Under the second law $\dot{\theta} = 0$ when $V = 0$; that is, θ evolves with slip alone. Both laws

[1]Institute of Geophysics, ETH Zurich, Switzerland.
[2]Department of Geosciences, Princeton University, Princeton, New Jersey, USA.

0148-0227/08/2007JB005082$09.00

Table 1. Notation

Parameter	Description
a; b	Coefficients of the rate-and-state direct and evolution effects
$C_{\Omega\gg1}$	Coefficient of fixed-length nucleation (equations (19) & (23))
$C_{\Omega\sim1}$	Coefficient of crack-like nucleation (equations (33) & (37))
C'	Coefficient of slip-law nucleation (equation (42))
D_c	Characteristic slip distance in the evolution law
G	Energy release rate
G_c	Fracture energy
h^*	Classical estimate of the nucleation length (equation (11))
k; k^*	Stiffness; effective crack stiffness
k_{cr}	Critical stiffness for instability
L	Half-length of the nucleation zone
L_b	Dieterich nucleation length scale (equation (12))
L_v	Fixed nucleation half-length (equation (22))
$L_{\min}$	Minimum nucleation half-length (equation (11))
L_∞	Asymptotic nucleation half-length (equation (32))
R	Length of the slip-weakening region
t^*	Time of instability
V	Slip speed
V_{bg}	Slip speed that at steady-state would and give rise to the ambient shear stress
V_{max}	Maximum slip speed behind the propagating front
V_{prop}	Propagation speed of the nucleation front
W	Width of the slip-law pulse (tip to peak slip)
x'	Distance behind the propagating front
δ	Slip distance
δ_c	Critical slip distance in fracture energy expression
Γ	$\ln(V_{max}\theta_i/D_c)$; proportional to $\Delta\tau_{p\text{-}r}$
θ	State variable in rate-and-state friction
θ_i	Value of θ ahead of the propagating front
μ'	μ (anti-plane strain) or $\mu/(1-\nu)$ (plane strain), where μ is shear modulus and ν is Poisson's ratio
Ω	$V\theta/D_c$; a measure of proximity to steady state
σ	Normal stress
τ	Shear stress
τ^∞	Shear stress that would act in the absence of slip
$\Delta\tau$	Average stress drop in the nucleation zone
$\Delta\tau_{p-r}$	Strength drop at the propagating front

exhibit steady state behavior ($\dot\theta = 0$) when $V\theta/D_c = 1$. If one interprets D_c as a typical contact size [*Dieterich and Kilgore*, 1994], then at steady state θ represents a typical contact lifetime D_c/V. Because of this, and because of the behavior at $V = 0$ for the aging law, θ is sometimes thought of as contact age [e.g., *Dieterich and Kilgore*, 1996]. However, even for the aging law this simple interpretation breaks down if $V\theta/D_c$ differs from 0 or 1.

[4] In the vicinity of steady state, $\ln(V\theta/D_c) \approx V\theta/D_c - 1$ and the two laws are asymptotically identical. Far from steady state this similarity disappears. Figure 1 shows the stress evolution during hypothetical velocity-stepping experiments, of the sort that experimentalists conduct but with much larger velocity jumps, for both laws. The surface was sliding with velocity V_1 and state θ_1 prior to the jump, and the subsequent velocity V_2 is chosen to produce ratios

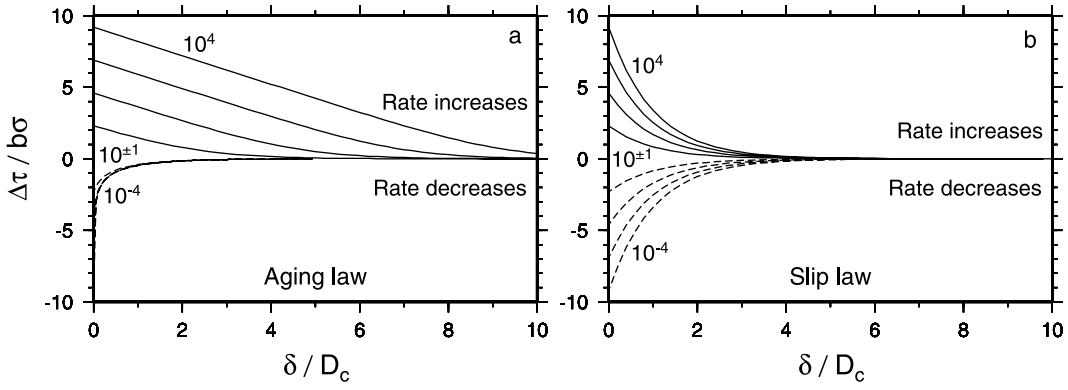

Figure 1. Plots of normalized stress as a function of normalized slip, for step velocity increases (solid lines) and decreases (dashed lines) of 1–4 orders of magnitude, for (a) the aging law and (b) the slip law. Stresses are relative to the future steady state value. For the aging law the curves for step decreases of 2–4 orders of magnitude appear indistinguishable, but they intersect the vertical axis at the same values of $\Delta\tau$ as for the slip law.

θ_1/θ_2 of $\pm 1-4$ orders of magnitude, where $\theta_2 \equiv D_c/V_2$ is the future steady state value (these are equivalent to velocity jumps of $\pm 1-4$ orders of magnitude if at the time of the jump the surface had been sliding at steady state). For constant V_2 equations (2) and (3) can be integrated to yield

$$\theta = \theta_2 + (\theta_1 - \theta_2)e^{-\delta/D_c} \qquad \text{(Aging law);} \quad (4)$$

$$\theta = \theta_2(\theta_1/\theta_2)^{\exp(-\delta/D_c)} \qquad \text{(Slip law);} \quad (5)$$

where δ is slip since the velocity jump. Substituting into (1), relative to the future steady state value τ_2 the stress is

$$\tau - \tau_2 = b\sigma \ln\left[1 + \frac{(\theta_1 - \theta_2)e^{-\delta/D_c}}{\theta_2}\right] \qquad \text{(Aging law);} \quad (6)$$

$$\tau - \tau_2 = b\sigma \ln(\theta_1/\theta_2)e^{-\delta/D_c} \qquad \text{(Slip law).} \quad (7)$$

Independent of the evolution law, the stress immediately following the velocity jump exceeds the future steady state value by $b\theta \ln(\theta_1/\theta_2)$ (independent because the steady state values are the same and as of yet there has been no evolution).

[5] For the aging law the following approximations accurately describe the stress evolution following large velocity increases and decreases, respectively:

$$\tau - \tau_2 \approx b\sigma[\ln(\theta_1/\theta_2) - \delta/D_c], \qquad \theta \gg \theta_2; \quad (8)$$

$$\tau - \tau_2 \approx b\sigma \ln\left[1 - e^{-\delta/D_c}\right], \qquad \theta \gg \theta_1. \quad (9)$$

The asymmetric response (Figure 1a) derives from the relative importance of time-dependent healing. For large velocity increases $V_2\theta_1/D_c \gg 1$, the constant term in (2) is initially negligible, θ evolves with slip but not time, and τ decreases linearly with slip according to (8). For large velocity decreases $V_2\theta_1/D_c \ll 1$, so θ initially evolves linearly with time and substantial evolution occurs over slip distances $\delta/D_c \ll 1$.

[6] It has long been recognized that velocity-stepping experiments exhibit rather symmetric behavior in response to velocity increases and decreases, consistent with the slip law [e.g., *Blanpied et al.*, 1998]. However, in other ways this law is deficient. Using a servo-control system to alter the effective stiffness of their testing apparatus, *Beeler et al.* [1994] found evidence that the frictional surface heals with time, rather than with ever-decreasing slip rate, during "slide-hold-slide" experiments. In addition, *Dieterich and Kilgore* [1994] observed microscopically that the true contact area increases with time during the stationary contact of two surfaces, presumably as a result of time-dependent deformation of asperities. Because the slip law is unable to account for this observed time-dependence, it appears that the aging law has become the law of choice among modelers over the last decade. It is also the case that most velocity-stepping experiments have been restricted to jumps of a single order of magnitude, where the asymmetric response of the aging law is somewhat subdued. However, our simulations suggest that it is the response of the fault surface near to and well above steady state that most strongly influences nucleation, and not the response well below steady state where the slip law appears to be inadequate. The response well above steady state is important because growing nucleation zones impose large and abrupt velocity increases in areas that were previously nearly locked, e.g., as a result of a prior earthquake. As we will show, the effective fracture energy of such a nucleation front is well-approximated by the area under the appropriate curve in Figure 1. This fracture energy in turn controls the nucleation style, which may differ markedly for the two evolution laws (Figure 2).

[7] Equations (1)–(3) have received considerable attention in the context of spring-block sliders ($\dot{\tau} = k[V^* - V]$, where k is the spring stiffness, V^* is the load-point velocity, and dots denote time derivatives). For the aging law, a necessary but not sufficient condition for instability, in the sense that neglect of inertia leads to infinite slip speeds, is that $a < b$; that is, that the surface be steady state velocity weakening. *Ranjith and Rice* [1999] showed that for arbitrary perturbations from steady state, instability also requires that the spring stiffness be less than a critical value given by

$$k_{cr} = \frac{\sigma(b-a)}{D_c}. \quad (10)$$

Because the two laws are asymptotically identical near steady state, for infinitesimal perturbations from steady sliding the same k_{cr} applies to the slip law. However, nonlinear stability analysis for the slip law indicates that for sufficiently large perturbations instability is possible for $k > k_{cr}$ [*Gu et al.*, 1984]. This property of the slip law has implications for nucleation on deformable faults, even under slow background loading, because the evolving nucleation zone provides its own large perturbation.

[8] The concept of a unique critical stiffness does not have a simple extension to deformable faults. Nonetheless, the following dimensional estimate is instructive. The effective stiffness at the center of a 2-D elastic crack (the stress drop for a given slip) is $k^* \equiv \Delta\tau/\delta = \mu'/2L$, where $2L$ is the crack length and μ' is the shear modulus μ for anti-plane strain and $\mu/(1-\nu)$, where ν is Poisson's ration, for plane strain. Setting this k^* equal to k_{cr} for a spring-block slider leads to the following estimate for the minimum half-length of a nucleation zone capable of instability:

$$L_{min} \sim \frac{1}{2}\frac{\mu' D_c}{(b-a)\sigma}. \quad (11)$$

To within a constant coefficient this is the critical size h^* introduced by *Rice* [1993]. Somewhat surprisingly, in a numerical study of the aging law *Dieterich* [1992] found that nucleation zones localized to a fixed length that scaled as b^{-1}, rather than $(b-a)^{-1}$, when $V\theta/D_c$ was much greater than 1. For $V\theta/D_c$ closer to steady state, on the other hand, the nucleation zone expanded during the approach to

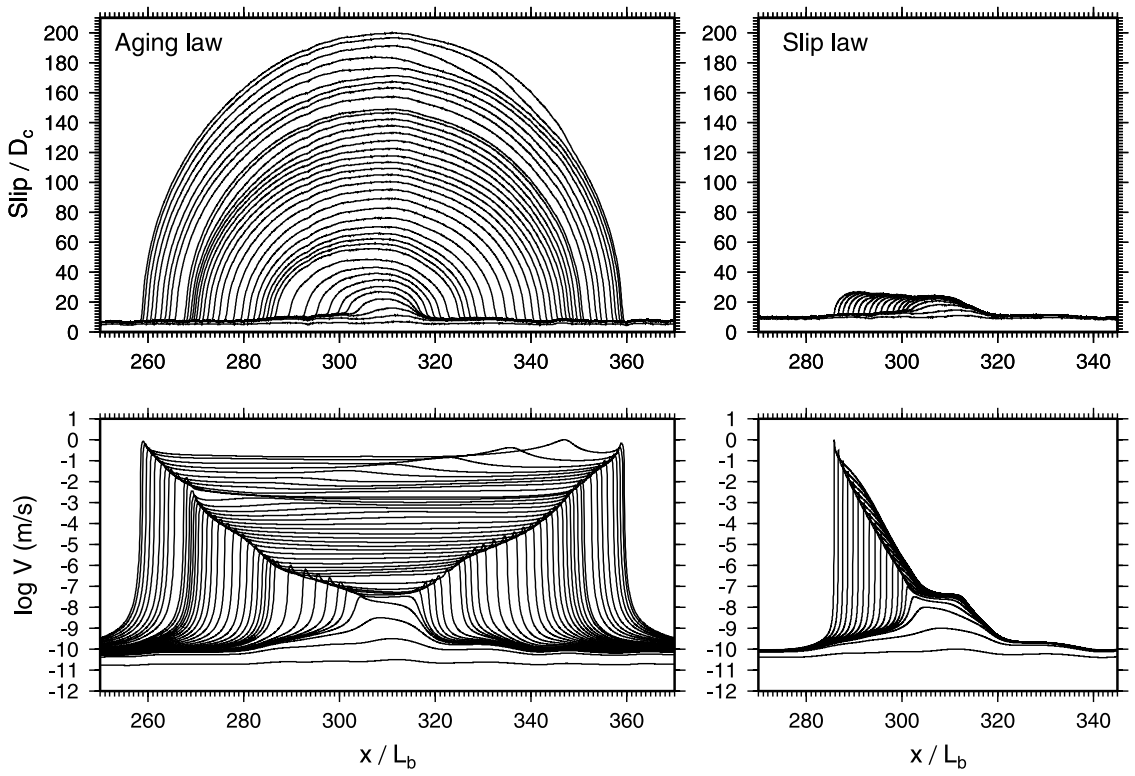

Figure 2. Snapshots of normalized slip (top panels) and slip speed (bottom) for two simulations identical in all respects except that the left panels use the aging law and the right panels the slip law. $a/b = 0.95$. The normalizing length scale $L_b \equiv \mu' D_c/b\sigma$. The grid spacing is $L_b/74$; initial and boundary conditions and material parameters are otherwise identical to those in Figure 3.

instability. Because the following terms occur repeatedly in this paper, we define

$$L_b \equiv \frac{\mu' D_c}{b\sigma}; \tag{12}$$

$$\Omega \equiv \frac{V\theta}{D_c}. \tag{13}$$

For $\Omega > 1$ the fault is above steady state and would weaken at constant slip speed, whereas for $\Omega < 1$ the fault is below steady state and would strengthen at constant slip speed. Throughout this paper we use "steady state" to mean $\Omega = 1$, without implying anything about the slip speed relative to the driving or plate rate.

[9] *Rubin and Ampuero* [2005a] obtained analytical estimates for the nucleation length and time-to-failure for deformable faults obeying the aging law. They identified two regimes, distinguished by the behavior of Ω: Well above steady state ($\Omega \gg 1$) everywhere, the regime emphasized by *Dieterich* [1992], and well above steady state only at the margins of the nucleation zone, with sliding being slightly above steady state ($\Omega \gtrsim 1$) in the interior. Well above steady state, nucleation localizes to a fixed length close to L_b, as found by Dieterich. A separable solution for this regime shows that only for $a/b < 0.3781$ does Ω increase during the approach to instability. For larger values, Ω is eventually driven down to an a/b-dependent value near 1. In this regime nucleation zones expand quasi-statically and asymptotically approach a value proportional to $[b/(b-a)]^2 L_b$, although how closely they approach this value before reaching dynamic slip speeds depends upon the loading conditions.

[10] Laboratory values of a/b are typically larger than 0.5, and a reasonable median value appears to be 0.9 even on velocity-weakening surfaces [*Kilgore et al.*, 1993; *Blanpied et al.*, 1998 using $a/(b_1 + b_2)$ for their 2-state-variable fits of the latter]. Near the base of the seismogenic zone, where loading rates are high and many large earthquakes seem to nucleate, a/b is expected to be close to 1 if, as is believed, this region marks the transition from velocity-weakening to velocity-strengthening behavior. The nucleation length for $a/b = 0.95$ can exceed that of the fixed-length solution by a factor of 100. For lab values of a and b ($\sim$0.01) and D_c near the upper end of laboratory measurements ($\sim$100 μm [*Marone*, 1998]), such a nucleation zone could be more than 1 km across, raising the possibility that it could be detected remotely. However, this large size is directly traceable to the large area beneath the aging law stress-displacement curves in Figure 1a. As was noted by *Nakatani* [2001], this prediction of the aging law is contradicted by laboratory experiments. Therefore in this paper we explore the slip law, which we find exhibits the same two general nucleation regimes, if not the same behavior. We begin by briefly reviewing and slightly extending the aging law results of Rubin and Ampuero, because these are useful for interpreting the slip law

simulations. The latter have proven to be more resistant to simple analytical approximations.

2. Numerical Method

[11] In the quasi-static limit we equate the frictional strength with the fault stress, which is partitioned into a boundary condition τ^{∞} and an elastic component τ^{el} due to nonuniform slip. In two dimensions the static elastic stresses are proportional to the Hilbert transform $\mathcal{H}$ of the along-fault slip gradient δ':

$$\tau(x) = \tau^{\infty}(x) + \tau^{el}(x) = \tau^{\infty}(x) + \frac{\mu'}{2}\mathcal{H}[\delta'](x) \tag{14}$$

Equating (1) and (14) and differentiating with respect to time yields

$$a\frac{\dot{V}}{V} + b\frac{\dot{\theta}}{\theta} = \frac{\dot{\tau}^{\infty}}{\sigma} + \frac{\mu'}{2\sigma}\mathcal{H}[V']. \tag{15}$$

The parameters σ, a, b, and $\dot{\tau}^{\infty}$ are taken to be constant and uniform. Equations (15) and (2) or (3) are solved using the numerical scheme of *Rubin and Ampuero* [2005a]. For growing nucleation zones the propagating front remains well above steady state, with the result that the smallest length scale to be resolved numerically scales roughly as L_b for the aging law and L_b divided by the logarithm of the velocity jump for the slip law. For the slip law at near-dynamic speeds this is much smaller than the critical cell size $h^* \sim \mu' D_c/\sigma(b\text{-}a)$ introduced by *Rice* [1993] (by a factor of $\sim$100 for $a/b = 0.75$). We settled on grid spacings of $L_b/50$–$L_b/150$, which for the aging law is finer than necessary. Simulations were carried out in double precision because for the slip law single precision sometimes gave rise to asymmetric nucleation from symmetric initial and boundary conditions. We use $D_c = 400$ μm, $\mu' = 11.56$ GPa, $\sigma = 100$ MPa, and $b = 0.01$. As we present results with lengths normalized by L_b and slips by D_c these choices are largely irrelevant (they influence the simulations only through the scaling of the initial or boundary conditions).

3. Aging Law Nucleation

3.1. Well Above Steady State

[12] For low values of a/b, the nucleation zone accelerates at fixed length while maintaining $\Omega \gg 1$ (e.g., Figure 1 of *Rubin and Ampuero* [2005a]). The latter observation motivates approximating the aging law (2) as

$$\dot{\theta} = -\Omega \tag{16}$$

[*Dieterich*, 1992]. The similar appearance of successive velocity profiles suggests a separable solution of the form

$$\begin{aligned} V(x,t) &= V_o(t)\mathcal{V}(x/L), && |x| < L; \\ V(x,t) &= 0, && |x| \geq L, \end{aligned} \tag{17}$$

$$\dot{\tau}^{el}(x,t) = V_o(t)\frac{\mu'}{2L}\dot{\mathcal{T}}(x/L), \tag{18}$$

where L is the fixed effective crack length, the velocity distribution $\mathcal{V}$ is a function of dimensionless position x/L, normalized such that $\mathcal{V}(0) \equiv 1$, and $\dot{\mathcal{T}}$ is the elastic stressing rate. Substituting (16)–(18) into (15), *Rubin and Ampuero* [2005a] obtained a solution with the following properties:

[13] (1) For slip speeds large enough that the remote loading rate is negligible ($\dot{\tau}^{el} \gg \dot{\tau}^{\infty}$), V_o evolves according to

$$\frac{\dot{V}_o}{V_o^2} = \frac{b}{a}\left[1 + \frac{L_b}{2L}\dot{\mathcal{T}}(0)\right]\frac{1}{D_c} \equiv \frac{C_{\Omega\gg1}}{D_c}, \tag{19}$$

with solution

$$V_o(t) = \frac{D_c}{C_{\Omega\gg1}}\left(t^* - t\right)^{-1} \quad ; \quad t^* \equiv D_c/C_{\Omega\gg1}V_o(0). \tag{20}$$

For $C_{\Omega\gg1} > 0$, infinite velocities are reached at a finite time t^*.

[14] (2) $\mathcal{V}$ and $\dot{\mathcal{T}}$ are determined by using elasticity to solve

$$\mathcal{V} = 1 - \frac{L_b}{2L}\left[\dot{\mathcal{T}}(\xi) - \dot{\mathcal{T}}(0)\right], \quad \left|\xi \equiv \frac{x}{L}\right| \leq 1, \tag{21}$$

an eigenvalue problem that has solutions for all values of the dimensionless nucleation length L/L_b. Adding the constraint that the stresses outside the nucleation zone remain finite, expressed as a stress intensity factor equal to zero, fixes L and $C_{\Omega\gg1}$ to the unique values

$$L_{\nu} \approx 1.3774 L_b; \tag{22}$$

$$C_{\Omega\gg1} \approx 0.3781\frac{b}{a}. \tag{23}$$

[15] (3) For $\dot{\tau}^{el} \gg \dot{\tau}^{\infty}$, the evolution of Ω is given by

$$\frac{\Omega(\xi,t)}{\Omega(\xi,0)} = \left(\frac{V_o(t)}{V_o(0)}\right)^{1-\mathcal{V}(\xi)/C_{\Omega\gg1}}. \tag{24}$$

Equation (24) shows that Ω decreases with increasing slip speed for $\mathcal{V}(\xi)/C_{\Omega\gg1} > 1$. Because $\mathcal{V}$ is maximal at the crack center, Ω decreases most rapidly (if at all) at $x/L = 0$. Substituting $\mathcal{V}(0) = 1$ and (23) into (24), the nucleation zone remains well above steady state until instability only for

$$\frac{a}{b} < \sim 0.3781. \tag{25}$$

[16] It is instructive to compare (24) to the corresponding expression for a spring-block slider with stiffness k. Substituting into (15) $\dot{\theta} = -V\theta/D_c$ and $\dot{\tau} = -kV$ (the latter assuming negligible load-point velocity) leads to $C_{\Omega\gg1} = (b/a)[1 - kD_c/b\sigma]$. Equation (24) then becomes

$$\frac{\Omega(t)}{\Omega(0)} = \left(\frac{V(t)}{V(0)}\right)^{1-a\sigma/(b\sigma-kD_c)}. \tag{26}$$

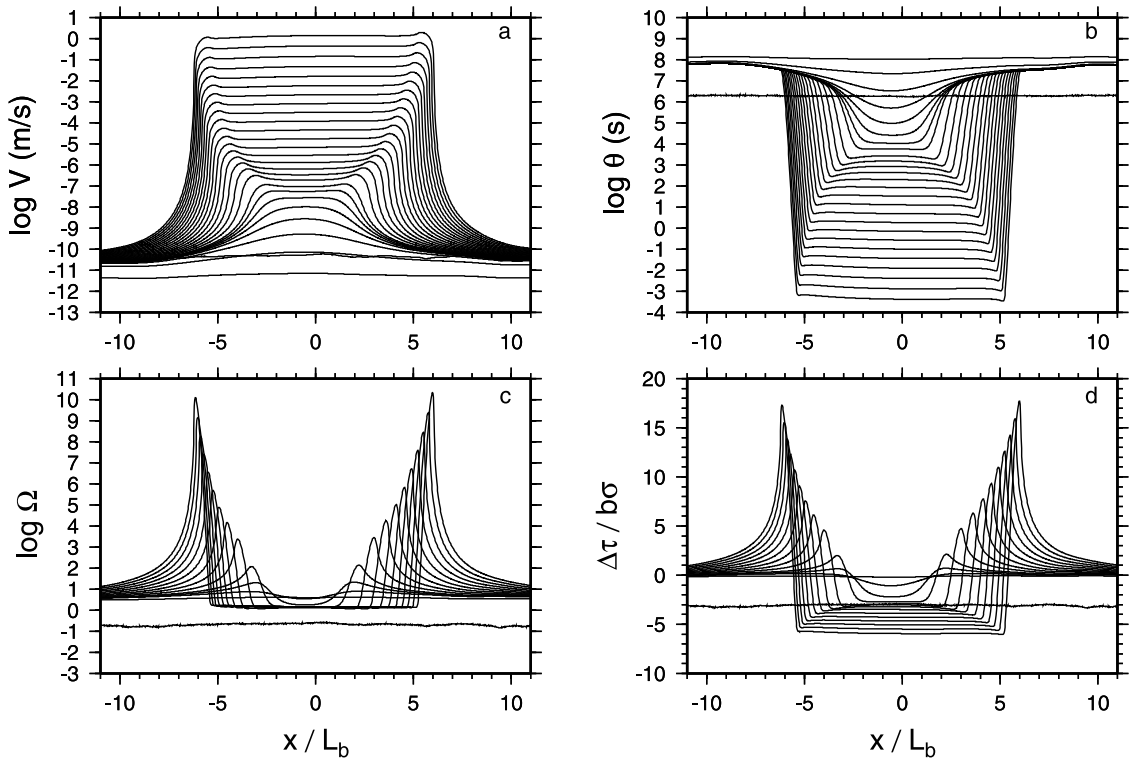

Figure 3. Snapshots from a simulation with a uniform initial slip speed of 10^{-9} m/s, an initial Ω randomly distributed between 0 and 1 on a grid spacing of 0.1 m ($\sim L_b/46$), and $\dot{\tau}^{\infty} = 10^{-2}$ Pa s^{-1}. a/b = 0.8. (a) Slip speed, (b) state, (c) $V\theta/D_c$, and (d) normalized stress change from the far-field average; for clarity Figures 3c and 3d show only every other profile. Note that while the nucleation zone expands these quantities are quasi-uniform in the interior, that Ω is quasi-constant as well, and that θ is not much perturbed until the arrival of the peak stress.

Examination of the exponent in (26) shows that the classical requirement for instability of a spring-block slider, $k \leq k_{cr} = (b-a)\sigma/D_c$, is identical to the requirement that Ω not decrease with increasing slip speed. For a deformable fault that is well above steady state, the interaction of the friction law with elasticity gives rise to an a/b-independent nucleation length with a maximum stiffness that is less than k_{cr} for $a/b < 0.3781$, and more than k_{cr} for $a/b > 0.3781$. This stiffness, reached at the crack center, is $0.6219(b\sigma/D_c)$.

3.2. Near Steady State

[17] We view the gross behavior of the nucleation zone as a competition between elasticity, which tends to smooth velocity variations and hence promote expansion, and the effective slip-weakening of the friction law, which favors localization. For $\Omega \gg 1$ these two tendencies apparently remain in balance and the nucleation zone accelerates at fixed length. For $a/b > 0.3781$, Ω increases as the fault passes through steady state from below, but then decreases as the nucleation zone begins to localize (because its effective stiffness is too large). As Ω approaches steady state, the slip-weakening rate in the interior of the nucleation zone decreases, tipping the prior balance in favor of elasticity, and the nucleation zone expands in a crack-like fashion.

[18] Figure 3 shows an example for a/b = 0.8. For a quasi-uniform stress drop $\Delta\tau$ within the interior of the nucleation zone (Figure 3d), the mechanical energy release rate G is

$$G = \frac{\pi}{2}\frac{L}{\mu'}\Delta\tau^2. \tag{27}$$

[*Lawn*, 1993]. The velocity jump experienced by material at the edge of the nucleation zone is sufficiently abrupt that the effective fracture energy G_c is essentially the area under the stress-vs.-displacement curves in Figure 1a. From equation (8), well above steady state the slip weakening rate is constant, $b\sigma/D_c$, so the effective slip-weakening distance δ_c increases linearly with the near-tip peak-to-residual stress drop $\Delta\tau_{p\text{-}r}$. This leads to

$$G_c = \frac{\Delta\tau_{p-r}\delta_c}{2} = \frac{D_c}{2b\sigma}\Delta\tau_{p-r}^2. \tag{28}$$

Setting $G = G_c$ and solving for the instantaneous nucleation length L,

$$L = \frac{L_b}{\pi}\left(\frac{\Delta\tau_{p-r}}{\Delta\tau}\right)^2. \tag{29}$$

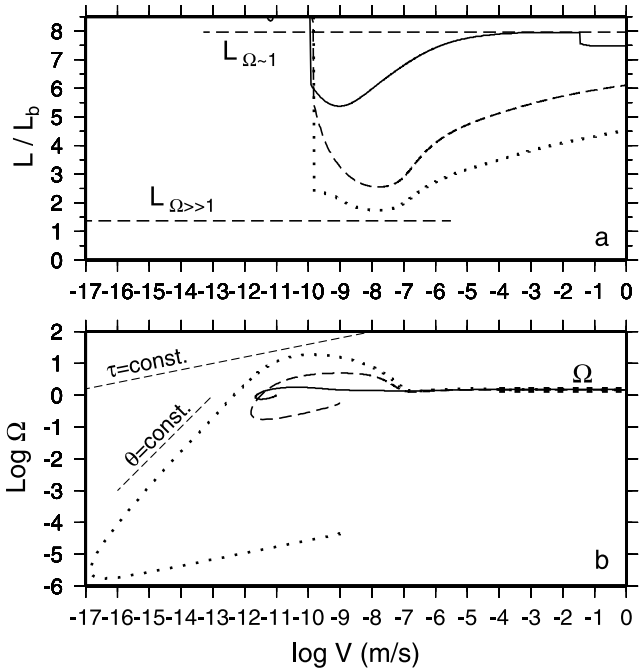

Figure 4. (a) Normalized nucleation length, defined as half the distance between the peaks in elastic stressing rate, and (b) $\log(V\theta/D_c)$, as functions of slip speed for 3 simulations with $a/b = 0.8$. The overall trend is for slip speed to increase with time. Dashed curve is for the simulation of Figure 3; dotted curve is for the identical conditions but with the initial Ω reduced by 4 orders of magnitude; solid curve is for a peaked load on an otherwise uniform surface initially slightly below steady state. The dashed and dotted lines labeled L_∞ and Ω refer to the predicted values for this a/b from equations (32) and (37). Note that Ω matches the prediction even for $L/L_\infty < 0.5$, reflecting the near-constant stiffness in (36). In Figure 4b, the upper and lower dashed lines parallel trajectories of constant stress and state, respectively.

[19] Accounting for the quasi-constant value of Ω in the nucleation zone (Figure 3c) leads to

$$\Delta\tau = \sigma\left[(b-a)\ln\left(V/V_{bg}\right) - b\ln(\Omega)\right] ; \tag{30}$$

$$\Delta\tau_{p-r} = b\sigma[\ln(V\theta_i/D_c) - \ln\Omega] ; \tag{31}$$

where V_{bg} is defined as the hypothetical background velocity which at steady state would give rise to the ambient stress τ^∞, and θ_i is the (relatively unperturbed) value of state ahead of the propagating nucleation front (Figure 3b). In the limit of large slip speeds the $\ln(\Omega)$ terms in (30) and (31) may be neglected, and $\ln(V\theta_i/D_c) \approx \ln(V/V_{bg})$. Thus the ratio $\Delta\tau_{p-r}/\Delta\tau$ approaches $b/(b-a)$, and the nucleation length is predicted to approach a limiting value L_∞ given by

$$L_\infty = \frac{L_b}{\pi}\left(\frac{b}{b-a}\right)^2 . \tag{32}$$

[20] A constant Ω implies $\dot{V}/V + \dot{\theta}/\theta = 0$. With $\dot{\theta} = 1-\Omega$ this leads to

$$\frac{\dot{V}}{V^2} = \frac{1-\Omega^{-1}}{D_c} \equiv \frac{C_{\Omega\sim1}}{D_c}. \tag{33}$$

Thus equation (20) from section 3.1 describes $V(t)$, but with a new definition of the constant. Substituting $-\dot{V}/V$ for $\dot{\theta}/\theta$ in (15), writing $-Vk^*$ for $\dot{\tau}$ and rearranging leads to

$$\frac{\dot{V}}{V^2} = \frac{k^*}{\sigma(b-a)} ; \tag{34}$$

equating this with (33) shows that the stiffness needed to maintain the given Ω is

$$k^* = \frac{\sigma(b-a)}{D_c}\left(1-\Omega^{-1}\right). \tag{35}$$

Note that this is smaller by the factor $(1-\Omega^{-1})$ than the critical stiffness for instability given in (10), but equals the critical stiffness for a spring-block slider with zero load-point velocity, as can be derived directly from equation (33) of *Ranjith and Rice* [1999].

[21] *Rubin and Ampuero* [2005a] neglected expansion of the nucleation zone and equated k^* with $\mu'/2L_\infty$, appropriate for a crack of fixed length L_∞. More properly, with $\delta = 2L\Delta\tau/\mu'$, $V = (2/\mu')(L\dot{\Delta\tau} + \dot{L}\Delta\tau)$, so

$$k^* = \frac{\dot{\Delta\tau}}{V} = \frac{\mu'}{2L_\infty}\left[\frac{L}{L_\infty} + \frac{\Delta\tau}{\dot{\Delta\tau}}\frac{\dot{L}}{L_\infty}\right]^{-1} . \tag{36}$$

We find that with G_c proportional to $\Delta\tau_{p-r}^2$, changes in $\Delta\tau$ and L are coupled such that the increased stiffness that comes from a smaller nucleation zone is offset, analytically to first order, by the decrease that comes from expansion (Appendix A). Thus the bracketed expression remains close to unity, and k^* varies by much less than L/L_∞. This helps explain Rubin and Ampuero's observation that time-dependent simulations begin tracking the predicted Ω quite closely well before L reaches L_∞ (Figure 4), and, as this is only a first-order result, their observation that the feedback maintaining the stiffness given by (35) is imperfect.

[22] Equating (35) with $\mu'/2L_\infty$ (now with greater justification) and combining with (32) leads to

$$C_{\Omega\sim1} \equiv 1-\Omega^{-1} \approx \frac{\pi}{2}\frac{b-a}{b} . \tag{37}$$

From (20), the time remaining to instability ($t^* - t$) is $C^{-1}D_c/V(t)$, or

$$t^* - t = \frac{2}{\pi}\frac{b}{b-a}\frac{D_c}{V(t)} . \tag{38}$$

Well above steady state, on the other hand, the comparable expression for the fixed-length solution is (from (20) and (23))

$$t^* - t = 2.645\frac{a}{b}\frac{D_c}{V(t)} . \tag{39}$$

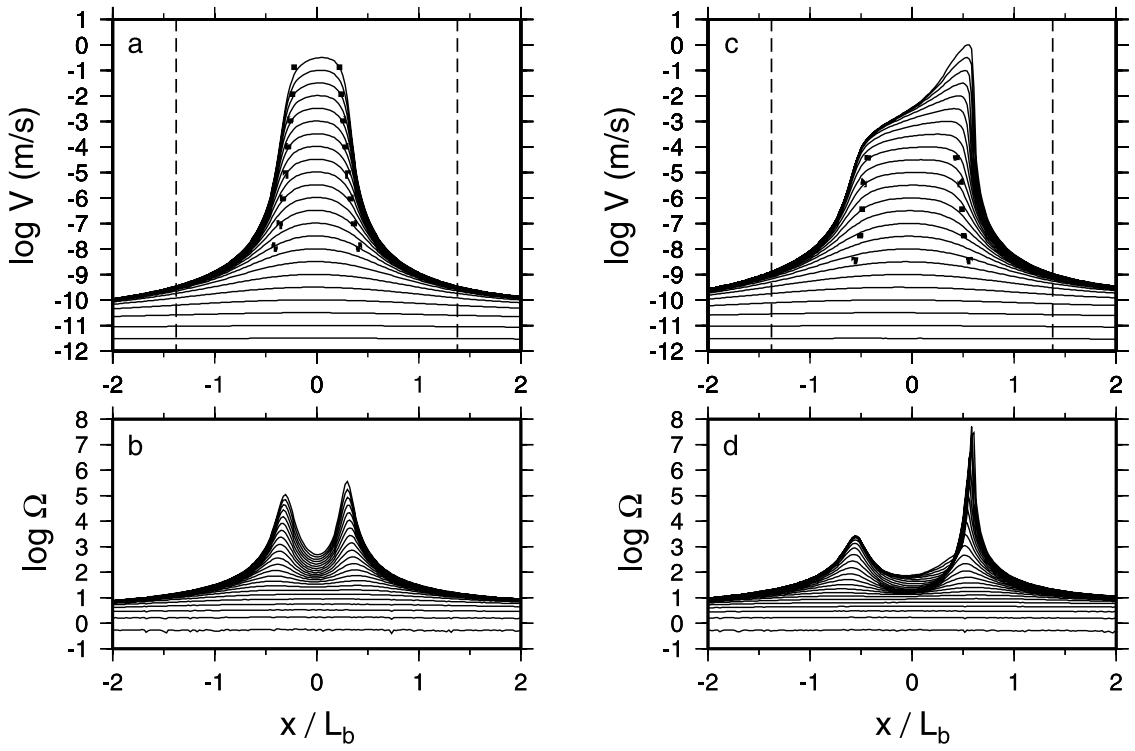

Figure 5. (a) and (b), Snapshots of slip speed and $V\theta/D_c$ from a slip-law simulation with $a/b = 0.5$; all other conditions are identical to those in Figure 3. Vertical dashed lines in Figure 5a indicate the nucleation length from the aging-law fixed length solution. The dotted lines are smaller by $\ln(\Omega)$, with Ω evaluated in the center of the nucleation zone. Figures 5c and 5d, The same but for $a/b = 0.6$. Ω in the interior begins to decrease before being increased by the stressing rate from the accelerating right margin.

Except for a/b very near to either 0 or 1, the time remaining to instability is of the order of D_c/V in both nucleation regimes.

[23] Equation (32) for L_∞ provides an excellent fit to the largest nucleation lengths in the simulations of *Rubin and Ampuero* [2005a] (their Figure 8a). For some boundary and initial conditions, on the other hand, the nucleation zone was smaller and still expanding when elastodynamic speeds were reached. A few examples are shown in Figure 4 for $a/b = 0.8$. The solid curve, which asymptotes to the predicted L_∞ before a little complexity sets in, is for a locally peaked initial load on an otherwise uniform surface. The dashed curve is for the simulation of Figure 3, and the dotted curve is for the identical conditions but with the initial values of θ reduced by 4 orders of magnitude. In general, as in Figure 4, we find that the minimum value of L reached during a simulation decreases as the maximum value of Ω reached during the onset of nucleation increases, although never to a value smaller than L_ν, and that L at a given slip speed decreases as this Ω_{max} increases because this delays the approach to the $\Omega \gtrsim 1$ solution.

4. Slip Law Nucleation

4.1. Well Above Steady State

[24] For $\Omega \gg 1$, so that the aging law becomes $\dot{\theta} \approx -\Omega$, the two evolution laws differ by the factor $\ln(\Omega)$. When substituted into (15), the resulting equations differ only in that $b\ln(\Omega)$ in the slip law replaces b in the aging law:

$$a\frac{\dot{V}}{V} - b\ln(\Omega)\frac{V}{D_c} = \frac{\dot{\tau}}{\sigma} \qquad \text{(Slip law);} \qquad (40)$$

$$a\frac{\dot{V}}{V} - b\frac{V}{D_c} = \frac{\dot{\tau}}{\sigma} \qquad \text{(Aging law, } \Omega \gg 1\text{).} \qquad (41)$$

Because of the logarithm, the factor $\ln(\Omega)$ in (40) may be regarded as a slowly varying correction to b in (41). Since L_ν for the aging law is inversely proportional to b, for the slip law the nucleation zone can be expected to be smaller by roughly $\ln(\Omega)$. Well above steady state, then, the nucleation zone slowly shrinks. This is shown in Figure 5a for $a/b = 0.5$. The dashed lines show L_ν, and the bold dotted lines $L_\nu/\ln(\Omega)$, with Ω evaluated at the center of the nucleation zone. The agreement with the numerical simulations is reasonably good, but because of the non-constant $\ln(\Omega)$ this scaling is not exact.

[25] The acceleration of slip is also somewhat different under the two laws. For the aging law in this regime $\dot{V}/V^2 = C_{\Omega\gg1}/D_c$, where the constant $C_{\Omega\gg1}$ is given by equation (23). For the slip law it is $\dot{V}/(V^2\ln\Omega)$ that remains approximately constant (Figure 6), as might have been

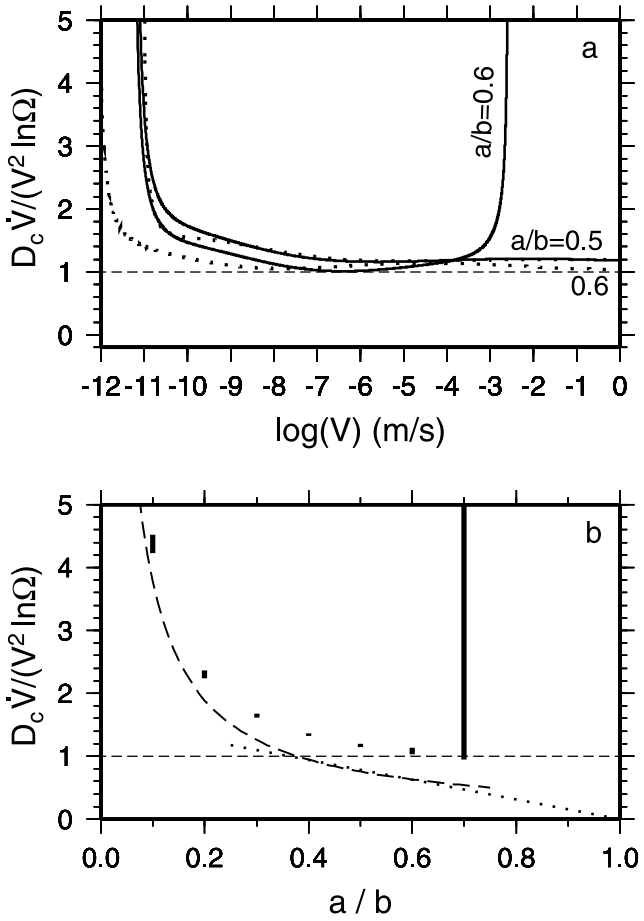

Figure 6. (a) $D_c\dot{V}/(V^2\ln\Omega)$ as a function slip speed, evaluated at the center of the nucleation zone, for a/b = 0.5 and 0.6. Solid curves are for the simulations in Figure 5; the curve for a/b = 0.6 reaches a minimum of 1.01 before leaving the $\Omega \gg 1$ regime. Dashed curves are for a locally peaked load on an otherwise uniform surface below steady state, subjected to a constant remote stressing rate. The curve for a/b = 0.6 reaches a minimum of 1.04 and remains in the $\Omega \gg 1$ regime. (b) Numerically determined values of $C' = D_c\dot{V}/(V^2\ln\Omega)$ as a function of a/b, for 2 series of simulations with a locally peaked load on an otherwise uniform surface. The two simulations were designed to access a range of $\Omega(V)$. The vertical bars indicate the full range of C' for slip speeds $10^{-3} < V < 10^4$ m/s. In general the difference between the two simulations is smaller than the variability within either, as with the a/b = 0.5 examples in Figure 6a. For a/b = 0.7 the simulations have left the $\Omega \gg 1$ regime. For comparison, the dashed curve shows $C_{\Omega\gg1} = D_c\dot{V}/V^2 = 0.3781b/a$ for the aging law, expected to be applicable for $a/b < 0.3781$, while the dotted line shows $C_{\Omega\sim1} = (\pi/2)(1 - a/b)$, applicable for larger a/b.

anticipated by substituting $b\ln\Omega$ for b in (19). By analogy with the aging law, we can define the (approximately) constant

$$C' = D_c \frac{\dot{V}}{V^2 \ln\Omega}. \tag{42}$$

From the identity $\dot{\Omega}/\Omega = \dot{\theta}/\theta + \dot{V}/V$ and the definition of the slip law,

$$\frac{\dot{\Omega}}{\Omega} = \frac{\dot{V}}{V} - \frac{V}{D_c}\ln\Omega. \tag{43}$$

Combining (42) and (43) and integrating leads to

$$\frac{\Omega}{\Omega_0} = \left(\frac{V}{V_0}\right)^{1-1/C'}, \tag{44}$$

where Ω_0 and V_0 are initial values. This is analogous to equation (24) for the aging law, so we expect the regimes $\Omega \gg 1$ and $\Omega \gtrsim 1$ to again be separated by $C' = 1$. We find empirically that C' for the slip law exceeds $C_{\Omega\gg1}$ for the aging law at a given a/b (Figure 6b), implying that the transition to the $\Omega \gtrsim 1$ regime occurs at larger a/b for the slip law, and also that C' approaches 1 more gradually than $C_{\Omega\gg1}$. Together with the fact that C' is slightly variable during any given simulation (Figure 6), this means that the transition to the $\Omega \gtrsim 1$ regime for the slip law occurs over a modest range of a/b. For the initial and boundary conditions of Figure 5 the transition begins between a/b = 0.5 and 0.6 (Figure 5c), whereas for 2 different manifestations of a locally peaked stress on an otherwise uniform surface it occurs for a/b between 0.6 and 0.7 (Figure 6b).

4.2. Near Steady State

[26] As with the aging law, for sufficiently large a/b the stiffness of the developing nucleation zone is large enough that the interior is either driven down toward or never gets far above steady state, and elasticity causes the nucleation zone to expand. Also, as with the aging law, the fault undergoes a sudden velocity increase as the edge of the nucleation zone sweeps by, with the result that the effective fracture energy is given to a good approximation by the area under the slip-vs.-displacement curves in Figure 1b. Integrating equation (7) to infinite slip distances yields

$$G_c = b\sigma \int_0^\infty \ln\left(\frac{V\theta_i}{D_c}\right) e^{-\delta/D_c} d\delta = b\sigma D_c \ln\left(\frac{V\theta_i}{D_c}\right); \tag{45}$$

integrating to only $3D_c$ recovers 95% of this value. That the fracture energy increases only as $\ln(V)$ while the energy release rate grows as $(\ln V)^2$ (equations (27) and (30)) means that, unlike the aging law, crack-like expansion is not an option. That is, in the limit of large slip speeds the energy balance $G = G_c$ for a hypothetical equilibrium crack becomes $L(\ln V)$ = constant, indicating that acceleration of slip is incompatible with growth of the nucleation zone.

[27] We find instead that nucleation takes the form of a unidirectional slip pulse. Examples are shown in Figure 7 for a/b = 0.8, 0.9, and 0.95. The initial and boundary conditions are identical for each panel; the direction of pulse propagation is presumably determined by the initial heterogeneity. Except for the slip-weakening zone, over the region the pulse has propagated the stress increases quasi-linearly with distance behind the propagating front (Figure 7, row 3). Such a stress distribution is consistent with elasticity, in that it represents a plausible smoothing of the $1/r$ stress perturbation associated with a dislocation. In conjunction

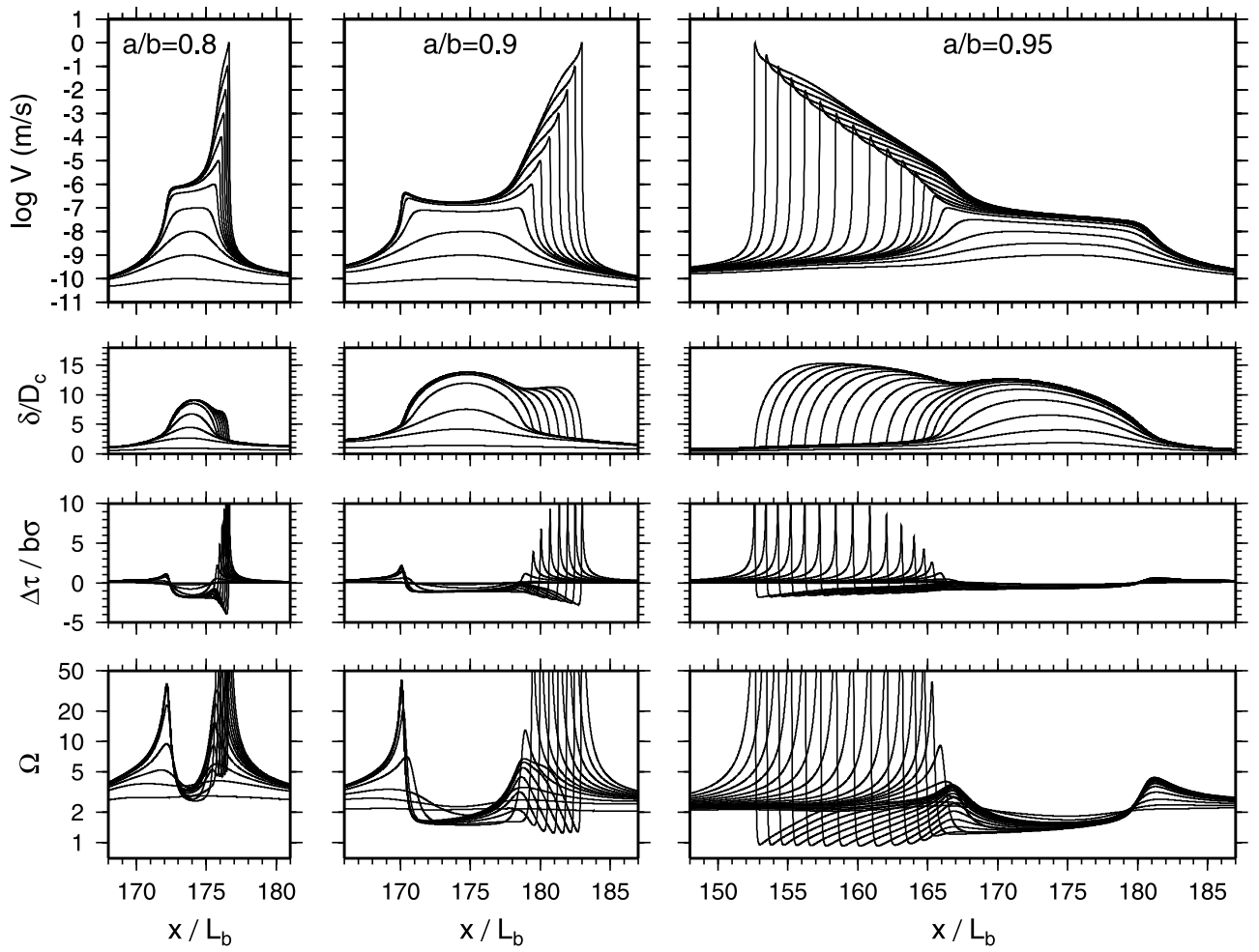

Figure 7. Snapshots from slip-law simulations with $a/b = 0.8$ (left column), 0.9 (middle column), and 0.95 (right column). Initial and boundary conditions are as in Figures 3 and 5, but using a smaller grid spacing of 3 cm ($\sim L_b/150$) to adequately resolve the nucleation front. Top row, slip velocity; second row, normalized slip accumulated since the first velocity snapshot; third row, normalized stress change; fourth row, $V\theta/D_c$.

with the friction law, such a stress distribution also requires that the pulse accelerate to instability. To see this, consider a hypothetical steady state pulse with a stress distribution $\tau(x')$ and slip distribution $\delta(x')$ that are independent of time, with x' being distance behind the tip. Then from the tail of the slip-weakening region to the location of peak slip $\dot{\tau}$ is positive, while V, always positive, is proportional to the slip gradient δ', and $\dot{V}$, proportional to δ'', is negative. With reference to equation (40), the second term on the left (the $b\dot{\theta}/\theta$ term) is negative when $\Omega > 1$, as for the examples in Figure 7, and even if Ω were less than 1 this term would be negligible near the peak slip, as δ' (that is, V) approaches zero. The $\dot{V}/V$ term, on the other hand, is negative wherever the slip distribution is concave downward. Thus equation (40) cannot be satisfied by a steady state pulse. For $\dot{\tau}$ to be positive, $\dot{V}$ must be positive, and this requires some combination of an ever-increasing slip gradient or propagation speed, either of which implies acceleration to instability.

[28] Note that although these nucleation zones are certainly pulse-like in a practical sense, they are not pulses in the strict sense of *Perrin et al.* [1995], who required $V = 0$ at some distance W behind the propagating front. *Freund* [1979] introduced slip pulses with a velocity distribution of the form $V(x') \propto [(W - x')/x']^{1/2}$, where x' is distance from the tip. Such pulses possess a discontinuity in dV/dx but no stress singularity at the healing front ($x' = W$). The pulses in Figure 7 are similar but possess a smoother "healing" front, followed by an exponentially decaying tail. Within the tail the slip speed is low enough that $\dot{\theta}/\theta$ is negligible, and $\dot{V}$ is determined by a local balance between $a\dot{V}/V$ and the positive $\dot{\tau}/\sigma$ that comes from propagation at the tip.

4.2.1. Pulse Shape

[29] In this section we use the estimated fracture energy to characterize the shape of the pulse front; in the following we use this to estimate the propagation speed. Near a crack tip but outside the slip-weakening zone,

$$\delta \approx \frac{4}{\sqrt{\pi}} \sqrt{\frac{G_c}{\mu'}} \sqrt{x'} \tag{46}$$

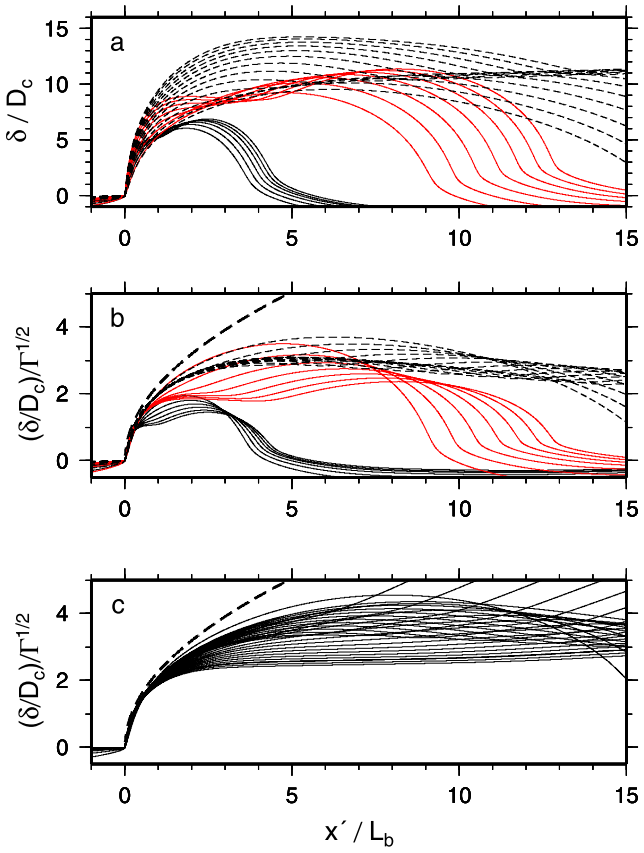

Figure 8. (a) Normalized slip as a function of distance behind the pulse tip for all snapshots in Figure 7 with $V_{max} > 10^{-5}$ m/s (for $a/b = 0.8$) and $V_{max} \geq 10^{-6}$ m/s (for $a/b = 0.9$ and 0.95). Slip has been offset to zero at the tip, and the horizontal axis has been reversed for $a/b = 0.8$ and 0.9. Dashed lines are for $a/b = 0.95$; red lines for $a/b = 0.9$. (b) The same slip profiles further normalized by $\Gamma^{1/2} \equiv [\ln(V_{max}\theta_i/D_c)]^{1/2}$. The bold dashed line shows the estimate from equation (47). (c) The same as Figure 8b but for the simulations of Figure 9 with $V_{max} > 10^{-7}$ m/s.

[*Lawn*, 1993]. Substituting the fracture energy from (45) and using the maximum slip speed V_{max} as the relevant velocity scale, (46) becomes

$$\frac{\delta}{D_c} \approx \frac{4}{\sqrt{\pi}} \left(\ln \frac{V_{max}\theta_i}{D_c} \right)^{1/2} \left(\frac{x'}{L_b} \right)^{1/2}. \quad (47)$$

That is, slip is expected to increase as the square-root of the distance behind the tip and to scale as $[\ln(V_{max}\theta_i/D_c)]^{1/2}$. Figure 8a shows δ/D_c as a function of x'/L_b for all slip profiles in Figure 7 corresponding to $V_{max} \geq 10^{-5}$ m/s (for $a/b = 0.8$) and $V_{max} \geq 10^{-6}$ m/s (for $a/b = 0.9$ and 0.95). The propagating front is identified as the interpolated location of peak stress. Slip has been offset to zero at the front, and the slip profiles for $a/b = 0.8$ and 0.9 have been reversed so that all the pulses apparently move to the left. As suggested by (47), Figure 8b further normalizes the slip by $[\ln(V_{max}\theta_i/D_c)]^{1/2}$, where θ_i is the largely unperturbed value of θ ahead of the propagating front. Whereas successive snapshots in Figure 8a increase in amplitude, the scaled profiles in Figure 8b decrease toward a relatively stable slip distribution over greater and greater distances behind the tip. The bold dashed curve shows the normalized slip estimate $(4/\pi^{1/2})(x'/L_b)^{1/2}$ from (47). The close agreement with the numerical profiles near the propagating front indicates that the fracture energy estimated from (45) is appropriate despite the non-constant velocity behind the front.

[30] In general, for a fracture tip propagating at equilibrium

$$G_c = G \propto \Delta\tau^2 W, \quad (48)$$

where the stress drop $\Delta\tau$ acts over the length scale W. We find that for the examples of Figure 7 the fracture energy balance $G_c \propto \ln(V_{max}\theta_i/D_c)$ is maintained by increasing $\Delta\tau$ within the pulse approximately as $\ln(V_{max}\theta_i/D_c)^{1/2}$ while the pulse width W (from tip to maximum displacement) remains roughly constant (e.g., at $\sim 5L_b$ for $a/b = 0.95$ and $\sim 1.5L_b$ for $a/b = 0.9$). This is consistent with the slip amplitude increasing roughly as $[\ln(V_{max}\theta_i/D_c)]^{1/2}$, as in Figure 8b. Both the pulse width and slip amplitude increase as a/b approaches 1.

[31] Despite the quasi-regular appearance of the velocity and slip profiles in Figures 7 and 8, we have thus far been unable to derive analytic approximations for the pulse width or slip amplitude as functions of a/b. Related to this, perhaps, there is more than one style of pulse capable of satisfying the fracture energy balance. Figure 9 shows examples where the initial conditions consist of a locally peaked stress on an otherwise uniform surface, subjected to a constant background loading rate. The simulations differ in a/b and in the length scale of the initial stress perturbation. In Figures 9a–9d, the slip amplitude remains roughly constant while the front continually steepens. In this case the fracture energy balance is maintained by increasing $\Delta\tau$ within the pulse as $\sim\ln(V_{max}\theta_i/D_c)$ while W shrinks as $\sim(\ln[V_{max}\theta_i/D_c])^{-1}$. In Figures 9e–9h, both the maximum slip and the pulse width increase very nearly as $\ln(V_{max}\theta_i/D_c)$, so the slip pulse appears nearly self-similar. The fracture energy balance is maintained by increasing W as $\sim\ln(V_{max}\theta_i/D_c)$ while $\Delta\tau$ remains essentially unchanged. For both pulse styles, however, the near-tip slip profile retains the scaling of equation (47) (Figure 8c).

[32] These differences in style are necessarily sensitive to the ambient conditions along the fault. For example, in Figure 7 (row 4) the minimum value of Ω behind the pulse tip is quasi-constant; this is also true of the example on the right in Figure 9 and, to a slightly lesser extent, of the example on the left. We find also that the slip speeds at these minima are a quasi-constant fraction of V_{max}. From the friction law this leads to $d\tau_{min}/d(\ln V_{max}) \approx$ constant, where τ_{min} is the stress minimum behind the tip (this occurs very close to the location of the minimum Ω). However, for $d\tau_{min}/d(\ln V_{max}) \approx$ constant to be consistent with values of $\Delta\tau$ that scale as various powers of $\ln(V_{max}\theta_i/D_c)$ (i.e., 0, 1/2, or 1) places requirements on the ambient stress. For example, for $\Delta\tau$ to be independent of V_{max}, as for the quasi-self-similar simulation in Figure 9, the ambient stress must decrease in parallel with $d\tau_{min}/d(\ln V_{max})$; that this is the case can be seen in Figure 9g.

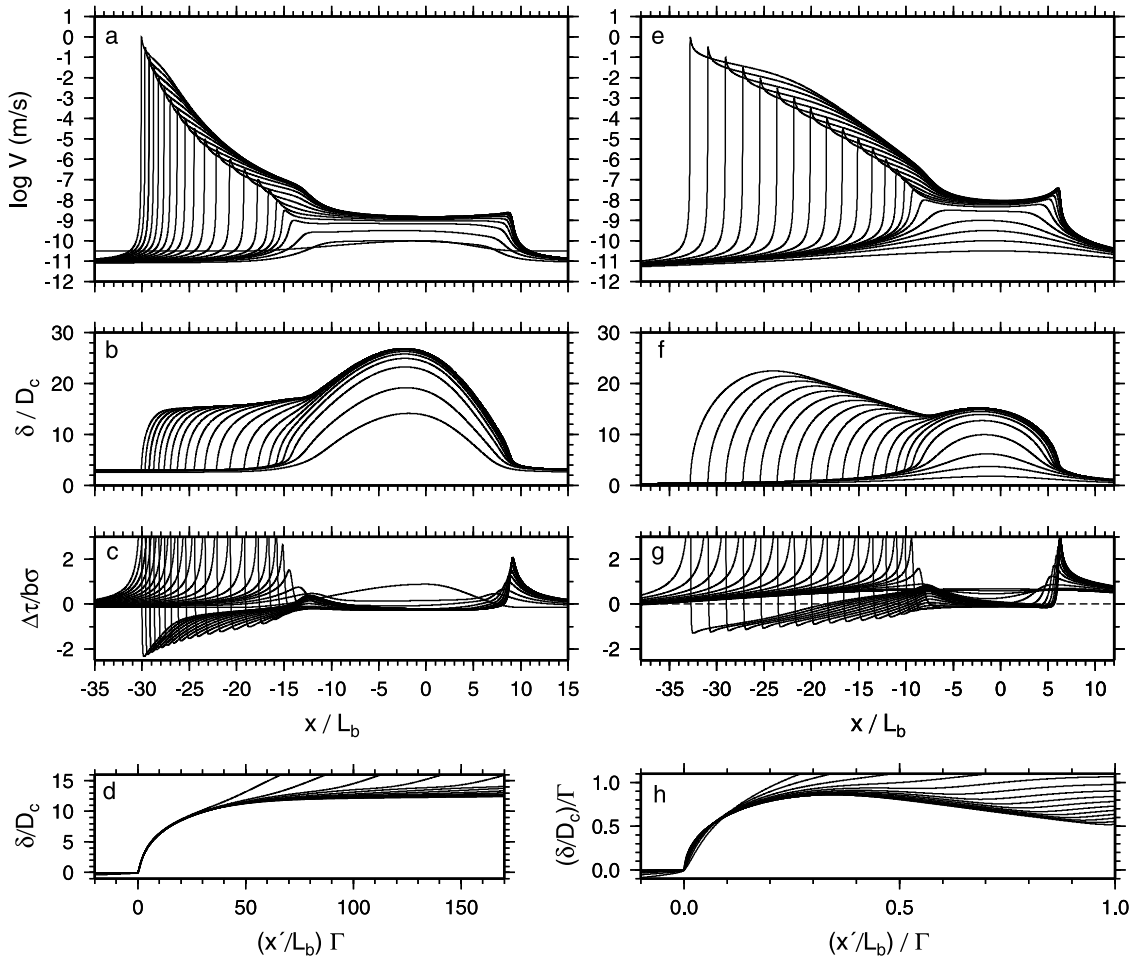

Figure 9. Snapshots of log slip speed (top row), normalized slip (second row), and normalized stress change from the local average (third row), for simulations with $a/b = 0.9$ (left column) and 0.95 (right). The initial conditions consist of a uniform state and a locally peaked, slightly asymmetric velocity over a length scale of $[b/(b\text{-}a)]L_b$, such that the fastest grid point is slipping at steady state. In Figure 9d, the slip profiles corresponding to $V_{max} \geq 10^{-7}$ m/s in Figure 9b have been shifted so that the tip sits at (0, 0) and the horizontal axis stretched by $\Gamma \equiv \ln(V_{max}\theta_i/D_c)$ (equation (51)). In Figure 9h, the slip profiles corresponding to $V_{max} \geq 10^{-7}$ m/s in Figure 9e have been normalized along both axes by Γ, and suggest an approach to self-similarity.

4.2.2. Propagation Velocity

[33] Close examination of the slip profiles shows that the length R of the slip-weakening region is shrinking. Dimensionally,

$$R \sim \delta_c \frac{\mu'}{\Delta\tau_{p-r}} \tag{49}$$

[*Rice*, 1980], where δ_c is the effective slip-weakening distance. Because $\Delta\tau_{p\text{-}r}$ increases roughly as $\ln(V_{max}/V_{bg})$ while δ_c is effectively fixed (Figure 1b), R decreases as $[\ln(V_{max}/V_{bg})]^{-1}$. In addition, because the stress profiles in Figure 1b are scaled versions of one another, the location of any particular $\delta \leq \delta_c$ scales by this same factor. This is shown in Figures 10a and 10b by the extent to which the slip profiles superimpose when the horizontal axis is stretched by $\ln(V_{max}\theta_i/D_c)$. Moreover, Figure 10e, which rescales all the slip profiles of Figures 8b and 8c, shows that very near the tip this shape is universal. The factor $\ln(V_{max}\theta_i/D_c)$ here ranges from about 10 to more than 20. Thus while the scaling of equation (47) and Figure 10a applies on a length scale that is somewhat less than the pulse width, on the still smaller scale of the slip-weakening region the scaling of Figure 10b applies. This shrinking of the slip-weakening region is what necessitates a very fine spatial grid to resolve slip-law nucleation fronts at large slip speeds.

[34] We can formalize the above, and as a corollary estimate the pulse propagation velocity, by writing that within the slip-weakening region

$$\frac{\delta(x,t)}{D_c} = s(\bar{x}), \tag{50}$$

where s is a function of dimensionless scaled position $\bar{x}$, defined as

$$\bar{x} \equiv \frac{x'}{L_b} \ln \frac{V_{max}\theta_i}{D_c}, \tag{51}$$

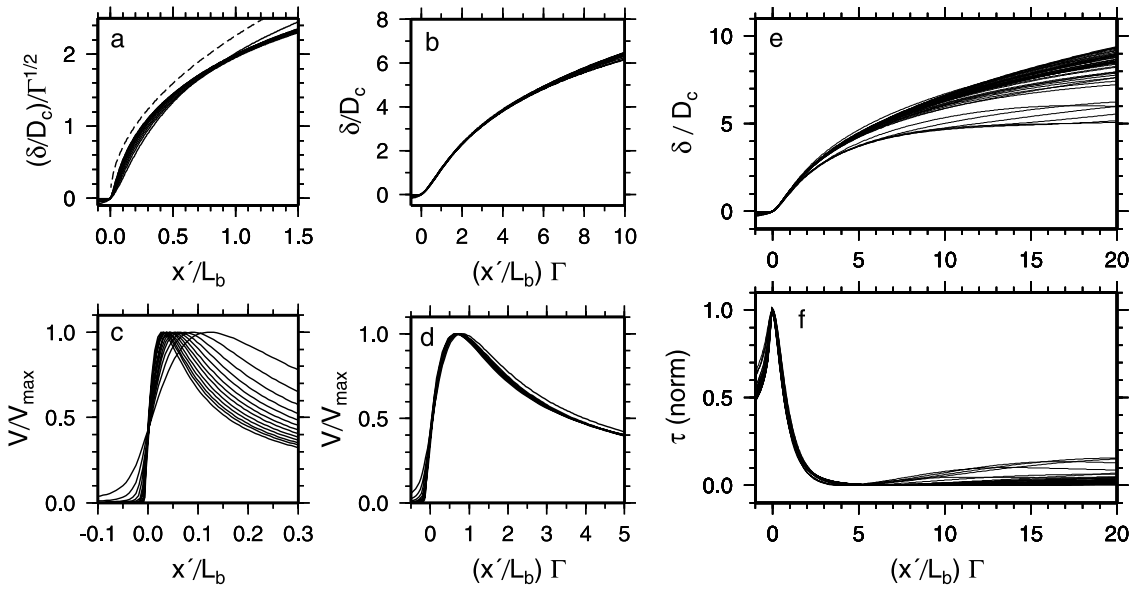

Figure 10. (a)-(d), Slip and velocity profiles for all the snapshots with $a/b = 0.95$ and $V_{max} \geq 10^{-6}$ m/s in Figure 7. (a) Normalized slip, scaled as suggested by equation (47), and (c), normalized slip speed, as functions of normalized distance behind the pulse tip. Dashed curve in Figure 10a shows the expected value of $(4/\pi^{1/2})(x'/L_b)^{1/2}$. (b) and (d), Normalized slip and slip speed as functions of normalized distance from the tip, with the latter stretched by $\Gamma \equiv \ln(V_{max}\theta_i/D_c)$ (equation (51)). The collapsing of all the profiles from Figures 10a and 10c shows that this is the appropriate scaling within the slip-weakening region. (e) Normalized slip as a function of scaled distance from the tip for all the slip profiles from Figures 8b and 8c, showing the universality of the near-tip slip profile. The cluster that deviates the most is for $a/b = 0.8$ in Figure 7. (f) The stress profiles corresponding to the slip profiles of Figure 10e, scaled from a peak value of 1 to a minimum of zero.

with x' being distance behind the front. Differentiating with respect to time, the slip speed is

$$\frac{V}{D_c} = \frac{ds}{d\bar{x}}\frac{d\bar{x}}{dt} = \frac{ds}{d\bar{x}}\left[\frac{V_{prop}}{L_b}\ln\frac{V_{max}\theta_i}{D_c} + \bar{x}\frac{\dot{V}_{max}}{V_{max}}\left(\ln\frac{V_{max}\theta_i}{D_c}\right)^{-1}\right], \tag{52}$$

where V_{prop} is the pulse propagation velocity and $\dot{V}_{max} \equiv dV_{max}/dt$. The first term in brackets represents the contribution from the translation of a time-invariant slip profile, and the second the contribution from a slip profile that steepens with time behind a stationary tip (due to the increasing V_{max}; in these examples $\dot{\theta}_i/\theta$ is negligible compared to $\dot{V}_{max}/V_{max}$). The rate of increase of V_{max} is slow enough that in all our simulations the slip speed is dominated, by at least 1–2 orders of magnitude, by the translation and not the steepening of the front (Appendix B). Dropping the latter term and evaluating (52) at $V = V_{max}$ yields

$$\frac{V_{prop}}{V_{max}} \approx 0.75\frac{\mu'}{b\sigma}\left(\ln\frac{V_{max}\theta_i}{D_c}\right)^{-1}, \tag{53}$$

where the coefficient 0.75 is the inverse of $ds/d\bar{x}$ taken from the numerical simulations at $V = V_{max}$, occuring at $\bar{x} \sim 0.7$ (Figure 10).

[35] Equation (53) suggests that V_{prop} increases with V_{max} but is independent of a/b. Thus the very different appearances of the pulses in Figure 7 are due not to slower propagation with decreasing a/b, but to more rapid acceleration of slip (so that there is less time for propagation, at the same V_{prop}, between neighboring slip speeds). This is confirmed in Figure 11, which shows that plots of V_{prop} versus V_{max} for the 5 simulations in Figures 7 and 9 are indistinguishable once the pulse is well-developed. The values of θ_i at the conclusion of these simulations vary by a factor of ~10, but at large $V_{max}\theta_i/D_c$ this amounts to differences in the logarithmic factor of only 10%.

[36] The essentials of equation (53) can be derived more transparently by starting with the assumption of a time-invariant slip profile [e.g., *Ida*, 1973]. In this case the maximum slip speed is given dimensionally by $\delta_c/(R/V_{prop})$, where the denominator is the timescale for passage of the slip-weakening zone. Substituting (49) for R leads to

$$\frac{V_{prop}}{V_{max}} \sim \frac{\mu'}{\Delta\tau_{p-r}} \sim \frac{\mu'}{b\sigma}\left(\ln\frac{V_{max}\theta_i}{D_c}\right)^{-1}. \tag{54}$$

For $\mu' = 40$ GPa, $\sigma = 40$ MPa, $b = 10^{-2}$, and the inverse logarithm of order 10^{-1}, V_{prop}/V_{max} is of order 10^4. The middle expression in (54) shows that this result is independent of the evolution law, as this affects only the path to steady state and not the total strength drop. In Appendix B we generalize the more complete equations (50)–(53) to fracture energies that scale as $(\ln[V/V_{bg}])^n$. By comparing the result for the aging law to an estimate derived by differentiating the time-dependent nucleation length, we gain insight into why, in the simulations of *Rubin*

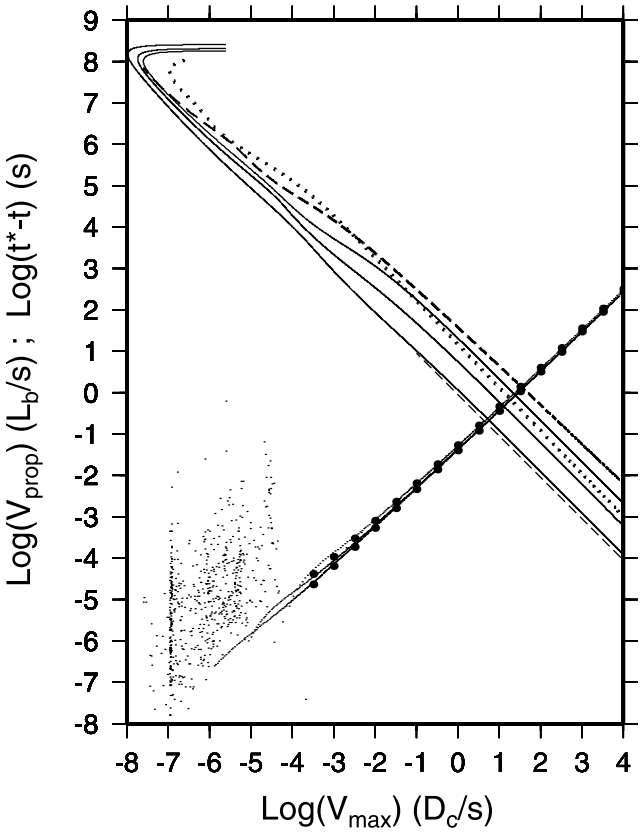

Figure 11. Log V_{prop} (ascending curves) and time to instability (t^*-t) (descending curves) for the 5 simulations of Figures 7 and 9, as functions of log V_{max}. The scatter in V_{prop} at low slip speeds occurs before the nucleation zone is well developed. The two merging bold-dotted curves give the estimates of V_{prop} from (53) assuming values of θ_i of 10^6 and 10^8 s, and show the insensitivity of V_{prop}/V_{max} to this parameter (θ_i typically increases from a few times 10^6 to a few times 10^7 s over this range of V_{max}). The 3 solid curves of (t^*-t) correspond, from lowest to highest, to a/b = 0.8, 0.9, and 0.95 in Figure 7; these end with slopes of -1 (lower dashed line), implying $\dot{V}_{max}/{V_{max}}^2$ = constant. The dotted and dashed curves of (t^*-t) correspond to a/b = 0.9 and 0.95 in Figure 9.

and Ampuero [2005a], V_{max} near the margin of the nucleation zone becomes substantially larger than V in the interior as a/b approaches 1.

[37] Equation (54) can also be used to judge whether the assumption of quasi-static elasticity is violated sooner by locally high slip speeds or by propagation of the slip pulse at near the shear wave speed. We can define V_{dyn} as the slip speed at which the local "radiation damping" term, $\dot{\tau}^{rad} = \dot{V}\mu/2c_s$ [*Rice*, 1993], becomes more important than the direct velocity effect in equation (15); the result is $V_{dyn} = 2a\sigma\, c_s/\mu$, where c_s is the shear wave speed. Substituting into (54) yields

$$\frac{V_{prop}/c_s}{V_{max}/V_{dyn}} \approx \frac{a}{b}\left(\ln\frac{V_{max}\theta_i}{D_c}\right)^{-1}. \qquad (55)$$

Because the logarithm may exceed 20 by the time V_{max} approaches V_{dyn} (with D_c/θ_i approximated as V_{plate} and V_{dyn} of order 0.1 m/s), we expect the applicability of quasi-static elasticity to be limited by the magnitude of the local slip speed rather than the propagation speed. Of course, other processes, such as frictional heating, may become important at even lower speeds [e.g., *Segall and Rice*, 2006].

4.2.3. Time to Instability

[38] For the simulations of Figure 7, Figure 11 shows that plots of the time remaining to instability ($t^* - t$) vs. V_{max} have slopes that are indistinguishable from -1, implying $\dot{V}_{max}/V_{max}^2$ = constant, just as in both aging law regimes. These curves are offset such that at the same V_{max} lower values of a/b reach instability sooner, as for the aging law. Qualitatively, following the arguments of section 4.2, this is consistent with the larger stress gradients behind the pulse tip for smaller a/b (Figure 7, row 3). That is, because the pulse propagation speed at a given V_{max} is independent of a/b, a larger stress gradient implies a larger $\dot{\tau}$, which in turn requires a larger $\dot{V}/V$.

[39] For the simulation of Figure 9e, $d(\ln V_{max})/dL$ = constant (the snapshots are plotted at equal increments of log V_{max} and show equal translations of the pulse front). Combining this with (53) shows that for this simulation $(\dot{V}_{max}/V_{max}^2)\ln(V_{max}\theta_i/D_c)$ = constant. For the simulation of Figure 9a, $(\dot{V}_{max}/V_{max}^2)[\ln(V_{max}\theta_i/D_c)]^{-1} \approx$ constant, reminiscent of the $\Omega \gg 1$ regime for the slip law. Note, however, that unlike the aging law in both regimes and the slip law for $\Omega \gg 1$ there is no fixed point that accelerates in this fashion; the point currently slipping at V_{max} has just been added to the pulse front.

[40] Compared to the total duration of nucleation, the slip-law pulses may be short-lived. For the simulation with a/b = 0.8 in Figure 11, ($t^* - t$) is within 10% of D_c/V_{max}. Thus if the pulse develops at $V_{max} \sim 10^{-6}$ m/s, as in Figure 7, it would persist for 400 s for D_c = 400 μm or 10 s for D_c = 10 μm. For the larger values of a/b in Figure 11, the pulses begin at somewhat lower slip speeds and might last 10–100 times longer. Missing from this analysis is a detailed understanding of how the initial conditions determine the slip speed at the onset of pulse formation, although this is certainly related to the decrease in Ω in the interior of the nucleation zone. The potential importance of the pulses is that they might be the only phase of quasi-static nucleation observable by near-source instruments.

4.2.4. "Nucleation Length" in Relation to the Critical Stiffness for Instability

[41] For the aging law, the region where the slip speed is well above background is more-or-less comparable to the region that is being elastically unloaded. This rough equivalence is generally assumed in any attempt to estimate the nucleation length from the critical stiffness of a spring-block slider. For the slip law in the near-steady state regime, this equivalence breaks down. At any moment only the tip of the slip pulse is being unloaded, on a spatial scale that varies from about 6 to 9 times $L_b/\ln(V_{max}\theta_i/D_c)$ as a/b varies from 0.8 to 0.95.

[42] The shrinking of the unloading region can also be viewed in terms of the competition between elasticity and slip-weakening. From equations (8) and (7), the instantaneous slip-weakening rate following a large step increase in sliding velocity is a constant $b\sigma/D_c$ for the aging law,

but is larger than this by $\ln(V_{max}\theta_i/D_c)$ for the slip law (Figure 1). The increase in slip weakening rate with increasing V_{max} is what promotes continued localization under the slip law. It is tempting to relate this also to the fact that slip-law spring-block sliders can reach instability for an arbitrarily large stiffness, given a sufficiently large perturbation from steady state [*Gu et al.*, 1984]. Such perturbations can of course be imposed externally, but Figures 7 and 9 show that they also arise naturally from nucleation itself, as the approaching slip pulse imposes a large stress perturbation on the fault immediately ahead. Once the slip-weakening zone passes by, this region continues to accelerate to instability (driven in part by the increasing stress due to slip near the current front), but much more slowly than the region at the front of the pulse where Ω is extremely large. Something similar happens in the $\Omega \gg 1$ regime, in that large values of Ω arising spontaneously during nucleation allow the nucleation zone to shrink to sizes several times smaller than that anticipated from a linear stability analysis.

5. Relation to Slow Transients

[43] Recently, periodic slow slip events have been identified near the base of the seismogenic portion of subduction zones in Cascadia and southwest Japan [*Dragert et al.*, 2001; *Obara and Hirose*, 2006]. Well-documented examples have total slips of $\sim$1–2 cm, extend several tens of kilometers down-dip, migrate along strike at rates of order 10 km/day, and have periodicities of $\sim$6–14 months. These events are of interest both from a seismic hazards standpoint and as a target for rate-and-state friction models. *Liu and Rice* [2005] observed "slow slip events" near the seismic/aseismic transition in 3-D numerical simulations using the aging law. The events were apparently constrained against instability because of prior earthquakes that had ruptured the full extent of the seismogenic region. The downdip extent of the transition from fully velocity-weakening to velocity-neutral behavior, about 5 km, was larger than both the fixed-length nucleation length $2L_\nu$ and the "classical" minimum length for instability $L_{\min}$, but smaller than the asymptotic crack length $2L_\infty$ ($\sim$10 km even in the fully velocity-weakening region). In principle the former could allow for nucleation while the latter might prevent acceleration to instability. For example, Ampuero and Perfettini [ms in preparation] ran cycle simulations with a velocity-weakening patch of length $2L$ embedded in a larger velocity-strengthening region, driven by a constant far-field velocity. They observed "periodic slow slip events" for $L_{\min} \lesssim L \lesssim L_\infty$ and instability (maximum slip speed limited by radiation damping) for $L \gtrsim L_\infty$. Our own simulations (unpublished), using a geometry more akin to a subduction zone (a velocity-weakening patch bordered by one locked and one velocity-strengthening region, as was carried out previously by *Liu and Rice* [2007] indicate that the corresponding boundaries are closer to $2L_{\min}$ and $2L_\infty$. Thus the expected range of patch lengths large enough for nucleation but too small for instability increases roughly in proportion to $b/(b - a)$, which becomes unbounded in the limit of velocity-neutral slip. Similar behavior occurs also in simulations using slip law, but over a much narrower range of patch lengths, as can be surmised from Figure 7.

[44] The slow events in the work of *Liu and Rice* [2005] had maximum slip speeds of $\sim 10^{-8}$–10^{-7} m/s, roughly 1–2 orders of magnitude above background, and propagated along strike at velocities of $\sim 10^{-4}$–10^{-3} m/s. Thus the ratio V_{prop}/V_{max} was roughly 10^4. The ratio $\mu'/b\sigma$ at the propagating front was 2×10^4. For $V_{max}\theta_i/D_c \sim 10^1$–$10^2$ the predicted ratio V_{prop}/V_{max} from (54) is 0.9–0.45×10^4. This factor of 2 or so agreement could be fortuitous, in that for slip speeds only 1–2 orders of magnitude above background the near-tip slip profile might not yet have reached its asymptotic distribution, but it is nonetheless encouraging.

[45] To consider a natural example, the August 1999 Cascadia event had $\sim$2 cm of slip over a downdip extent of 50 km, and propagated $\sim$300 km at $V_{prop} \sim 6$ km/day ($\sim$0.07 m/s) [*Dragert et al.*, 2001]. The maximum slip speed is not well constrained. The geodetic signal at individual GPS stations lasted from 6–15 days, yielding a nominal slip rate $V \sim 2 \times 10^{-8}$ m/s (2 cm/10^6 s), but if the slip speed were as peaked as for the slip-law examples in this paper, or the aging-law examples with $a/b \gtrsim 0.9$ in *Rubin and Ampuero* [2005a], the peak value could be several times larger and for slip at 30–40 km depth would likely be unresolved by surface stations. Arbitrarily multiplying the nominal value by 5 yields a maximum slip speed of $V_{max} \sim 10^{-7}$ m/s, about 10^2 times the plate convergence rate, and a ratio V_{prop}/V_{max} of $\sim 0.7 \times 10^6$. With $\mu = 30$GPa, $b = 0.01$, and $V_{max}\theta_i/D_c$ approximated as the ratio of the slip rate to plate rate (the logarithm makes the result rather insensitive to this estimate), equation (54) indicates that this ratio of V_{prop}/V_{max} implies an effective normal stress σ of 1 MPa. Although this is a very small value, it is of the same order as that advocated by *Liu and Rice* [2007] to match the observed 14-month periodicity of the Cascadia events. They argue that such small effective stresses might be produced by dehydration reactions in the subducting plate.

[46] Other rate-and-state considerations point to low effective stresses as well. The slip/length ratio is given by $\delta/2L \sim \Delta\tau/\mu'$; to reach 2 cm of slip over a length scale of 50 km requires a very low stress drop of 0.016 MPa for $\mu' = 40$ GPa. Approximating the rate-and-state stress drop as $\sigma(b - a)\ln(V/V_{bg})$, and taking $V/V_{bg} \approx 10^2$ and $(b-a) \approx 10^{-3}$, implies $\sigma = 3.5$ MPa. Stabilizing slip over a patch size of tens of kilometers is also aided by low values of σ, as all the relevant length scales are proportional to σ^{-1}. Using the aging law as an example, requiring $4L_\infty \gtrsim 50$ km and taking $b \approx 10^{-2}$, $(b-a) \approx 10^{-3}$, and $D_c \approx 40$ μm yields $\sigma = 0.5$ MPa. While these three estimates of σ are not identical, they are encouragingly close, given their order-of-magnitude nature, and uniformly low.

6. Which Evolution Law?

[47] Neither the aging nor the slip law matches all the available laboratory friction data. However, our simulations suggest that it is the behavior of the fault surface in the vicinity of and well above steady state that controls nucleation, and here the slip law seems clearly superior. *Nakatani* [2001] summarizes evidence that the effective slip-weakening distance following a velocity increase does not increase

with the magnitude of that increase. *Bayart et al.* [2006] describe more recent experiments on synthetic quartz gouge showing that velocity jumps of 1 and 2 orders of magnitude yield slip-weakening curves that are simply scaled versions of one another, behavior that is consistent with the slip law but not the aging law (Figure 1). Even the general observation that it is more difficult to stabilize large velocity jumps than small jumps on velocity-weakening surfaces in the laboratory is consistent with a slip-weakening rate that increases with the magnitude of the velocity jump, behavior that is predicted by the slip law but not the aging law.

[48] *Beeler et al.* [1994] found evidence for time-dependent, as opposed to slip-dependent, healing in slide-hold-slide experiments that access slip speeds and values of Ω that are considerably smaller than those typical of velocity-stepping tests. Such behavior, which is inconsistent with the slip law, is likely to be important during the interseismic period. Except insofar as this influences the slip speed and the degree of heterogeneity along the fault as it passes through steady state from below, however, it is not apparent that this would significantly influence nucleation. Of the three relevant length scales that have been identified thus far — L_ν, $L_{\min}$ or h^*, and L_∞ — none make reference to behavior well below steady state. Rather, their analytic approximations depend upon the behavior well above steady state (L_ν), near steady state ($L_{\min}$), or a combination of well above steady state at the margins and near steady state in the interior (L_∞). If an evolution law that permits time-dependent healing during the interseismic period is desired for earthquake cycle simulations, ad-hoc approaches are available. These include the "composite" law of *Kato and Tullis* [2001], which combines the slip law with healing at low slip speeds, or a linear combination of the two laws with more weight attached to the slip law [*Sleep*, 2005]. *Sleep* [2006] also presents micromechanical arguments outlining the conditions under which either the aging or slip law might apply.

7. Summary and Conclusions

[49] The slip and aging laws exhibit the same primary regimes of nucleation. Well above steady state, when $V\theta/D_c \gg 1$, the two laws are qualitatively similar. Under the aging law nucleation zones accelerate while maintaining a fixed length that is independent of a/b. Slip law nucleation zones are smaller than this by roughly $\ln(V\theta/D_c)$, and slowly shrink as instability is approached. For both laws, however, laboratory values of a/b favor nucleation near steady state, and here their behaviors differ markedly. This difference is controlled by the behavior at the propagating front(s), which remain well above steady state. That the fracture energy increases as $[\ln(V/V_{bg})]^2$ for the aging law means that nucleation takes the form of a quasi-statically expanding crack, whereas the increase as $[\ln(V/V_{bg})]^1$ for the slip law gives rise to an accelerating slip pulse.

[50] This difference is profound. For the aging law, with $a/b = 0.95$, $D_c = 100$ μm, and an effective normal stress of tens of MPa, the nucleation zone could be 1 km across, raising the possibility that it could be observed remotely. For the slip law this seems unlikely, the region of largest slip speeds being of order 100 times smaller. The smaller slip distances during slip-law nucleation (e.g., Figure 2) also seem likely to make thermal pressurization of pore fluid less important for the slip law than for the aging law [e.g., *Segall and Rice*, 2006].

[51] Dropping the effective normal stress to $\sim$1 MPa, as advocated by *Liu and Rice* [2007], could increase the aging law nucleation length to tens of kilometers. The large disparity between L_∞ and either L_ν or $L_{\min}$ for the aging law, particularly as a/b approaches 1, implies that there is a significant range of fault lengths capable of hosting slow slip events; that is, fault lengths large enough for an event to nucleate but too small for it to reach instability.

[52] Although for the slip law we have no analytical expression for a length scale comparable to L_∞, our simulations suggest that the range of fault lengths permitting slow slip events for the slip law would be much less. By the same reasoning, any physical process that increases the effective fracture energy of the nucleation front with increasing slip speed more rapidly than $(\ln[V/V_{bg}])^2$ would increase the range of fault lengths permitting such behavior. One plausible mechanism is inelastic dilation coupled with pore pressure reduction; because pore pressure recovery depends upon time and not slip, the effective slip-weakening distance in this case could increase quasi-linearly with slip speed, rather than logarithmically.

[53] For both laws, migrating nucleation fronts have a ratio of propagation speed to maximum slip speed of order $(\mu'/b\sigma)(\ln[V_{max}/V_{bg}])^{-1}$. The two velocities are related through the near-tip slip gradient, which is of order $\Delta\tau_{p-r}/\mu'$.

[54] Three-dimensional simulations indicate a complete carry-over of the behaviors seen in 2-D, with the slip-law pulses originating from either a mode-II or mode-III margin of the parent nucleation zone [*Rubin and Ampuero*, 2005b]. For the aging law, the transitional value of a/b in 3-D is $\sim$0.195, roughly half that in 2-D, and for the slip law, with modest heterogeneity along the fault the transition seems to begin by $a/b = 0.4$. Thus to the extent that laboratory evolution laws and rate-and-state parameters can be safely applied to the Earth, slip-law pulses might be the favored form of nucleation on natural faults. It must be borne in mind, however, that this requires extrapolation of experimental observations to much larger velocity increases than have ever been achieved in the laboratory, and that even within the range covered by experiment neither law satisfies all the data. Our simulations demonstrate how remarkably different nucleation can appear using two evolution laws that have each been advertised as "adequate" at some level.

Appendix A: Stiffness of the Expanding Aging-law Nucleation Zone

[55] That Ω is quasi-constant in the interior of the growing aging-law nucleation zone implies that the effective stiffness is a constant given by equation (35). The ability of the nucleation zone to maintain (approximately) this stiffness even as it expands seems surprising, but derives from interaction of elasticity with the friction law, as outlined below.

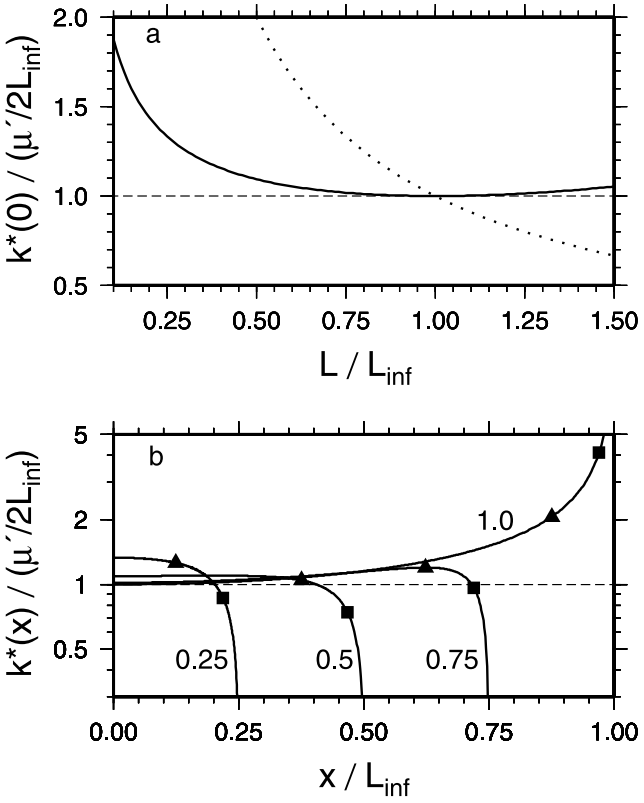

Figure A1. (a) Solid line, effective stiffness at the center of the growing nucleation zone, $k^*(0)$, normalized by the value for a crack of fixed half-length L_∞, as a function of normalized nucleation length L/L_∞ (equation A5). The broad minimum near 1 shows that $k^*(0)$ remains much closer to $\mu'/2L_\infty$ than to $\mu'/2L$ (dotted line). (b) Normalized stiffness as a function of position x/L_∞, for L/L_∞ = 0.25, 0.5, 0.75, and 1.0, showing that k^* remains close to $\mu'/2L_\infty$ over most of the growing nucleation zone as well (equation A7). Triangles and squares indicate a distance L_b behind the nucleation front for a/b = 0.8 and 0.9, respectively; larger values of x lie near or within the slip weakening region where equation (A7) is inappropriate.

[56] Equation (36) for the stiffness at the center of a crack with a uniform stress drop can be rewritten as

$$k^* = \frac{\mu'}{2L}\left[1 + \frac{\Delta\tau}{\dot{\Delta}\tau}\frac{\dot{L}}{L}\right]^{-1} . \tag{A1}$$

Taking the logarithm of (29), which combines the criterion for equilibrium crack growth with the aging-law estimates of $\Delta\tau$ and $\Delta\tau_{p-r}$, and then differentiating leads to

$$\frac{\Delta\tau}{\dot{\Delta}\tau}\frac{\dot{L}}{L} = 2\frac{\dot{\Delta}\tau_{p-r}}{\Delta\tau_{p-r}}\frac{\Delta\tau}{\dot{\Delta}\tau} - 2 . \tag{A2}$$

With Ω constant, equations (30) and (31) lead to

$$\frac{\dot{\Delta}\tau_{p-r}}{\dot{\Delta}\tau} = \frac{b}{b-a}, \tag{A3}$$

so (A2) becomes

$$\frac{\Delta\tau}{\dot{\Delta}\tau}\frac{\dot{L}}{L} = 2\frac{b}{b-a}\frac{\Delta\tau}{\Delta\tau_{p-r}} - 2 = 2\sqrt{\frac{L_\infty}{L}} - 2 , \tag{A4}$$

where the second equality makes use of the ratio $\Delta\tau/\Delta\tau_{p-r}$ from (29) and (32). Substituting (A4) back into (A1), we obtain

$$k^* = \frac{\mu'}{2L}\left[2\sqrt{\frac{L_\infty}{L}} - 1\right]^{-1} . \tag{A5}$$

This function has a broad minimum at $L = L_\infty$, implying that k^* remains close to $\mu'/2L_\infty$ even for L/L_∞ considerably less than 1 (Figure A1a).

[57] That Ω remains quasi-constant all the way to the slip-weakening zone implies that k^* remains close to $\mu'/2L_\infty$ over this entire region as well. For a stationary crack, the stiffness near the margins is greater than that at the center (the slip is less for a given stress drop), but propagation decreases the stiffness at the ends more than that at the center and these two effects tend to cancel. From equation (28) of *Rubin and Ampuero* [2005a], the slip speed within a growing crack subjected to a uniform but time-varying stress drop is

$$V(x) = -\frac{2}{\mu'}\left[\dot{\Delta}\tau L\left(1 - \frac{x^2}{L^2}\right)^{1/2} + \Delta\tau\dot{L}\left(1 - \frac{x^2}{L^2}\right)^{-1/2}\right] . \tag{A6}$$

Dividing by $\dot{\Delta}\tau$ and making use of (A4) leads to

$$k^*(x) = -\frac{\mu'}{2L_\infty}\left[\frac{L}{L_\infty}\left(1 - \frac{x^2}{L^2}\right)^{1/2} + 2\left(\sqrt{\frac{L}{L_\infty}} - \frac{L}{L_\infty}\right)\cdot\left(1 - \frac{x^2}{L^2}\right)^{-1/2}\right]^{-1} , \tag{A7}$$

where the bracketed expression now represents the deviation of the stiffness from the value needed to maintain the given Ω. Figure A1b plots this expression as a function of x/L_∞ for 4 values of L/L_∞: 0.25, 0.5, 0.75, and 1. The curve for L/L_∞ = 1 shows the increase in k^* near the margins of a stationary crack, while the others show the decrease near the margins of a propagating crack. The solid symbols indicate a distance of L_b behind the crack tip for a/b = 0.8 (triangles) and 0.9 (squares); (A7) is not expected to be accurate closer to the tip than this because of the nonuniform stresses within the slip-weakening region, which (A6) neglects. The tendency for points interior to this to plot near unity is indicative of the ability of the crack to maintain a near-constant and uniform stiffness as it grows. That this ability deteriorates as L/L_∞ approaches 1, especially for larger a/b, may explain much of the complexity seen in the simulations of *Rubin and Ampuero* [2005a]. This complexity increased with both a/b and L/L_∞.

[58] Equation (33) of *Ranjith and Rice* [1999] can be rewritten to show that the trajectory Ω = constant marks the stability boundary for a spring-block slider with zero load point velocity. In light of this, the above considerations

suggest what might happen when a growing aging law nucleation zone encounters barriers spaced more closely than $2L_\infty$. Because it can no longer expand and $L < L_\infty$, the nucleation zone stiffness will exceed the critical value needed to maintain the current Ω. It will then follow a trajectory of lesser acceleration than the Ω = constant case and (ultimately) deceleration to slip speeds low enough that the background loading rate again becomes important. For some of the initial and boundary conditions examined by *Rubin and Ampuero* [2005a], the nucleation zone reached elastodynamic speeds before L reached L_∞. However, for the cycle simulations of Ampuero and Perfettini [manuscript in preparation], with a velocity-weakening region of length $2L$ embedded in velocity-strengthening surroundings, elastodynamic speeds were not reached except for $L > L_\infty$.

Appendix B: Velocity of the Nucleation Front

[59] Here we generalize the expression for V_{prop}/V_{max} to fracture energies that scale as $(\ln[V/V_{bg}])^n$, and discuss the implications of two independent estimates of V_{prop} for the aging law. We continue to assume that the total strength drop is independent of the evolution law, so

$$\Delta\tau_{p-r} = b\sigma \ln\frac{V_{max}\theta_i}{D_c} \ , \tag{B1}$$

but allow for different slip-weakening distances

$$\delta_c = \Pi D_c \left(\ln\frac{V_{max}\theta_i}{D_c}\right)^{n-1} \ , \tag{B2}$$

where Π is some constant coefficient (e.g., 1 for the aging law, for which $n = 2$). We assume that within this slip distance $\Delta\tau/\Delta\tau_{p-r}$ is a function only of δ/δ_c (as is strictly true for the slip law [$n = 1$], and true for the aging law while $\Omega \gg 1$). From (49), the length of the slip-weakening zone is

$$R = \alpha\Pi L_b \left(\ln\frac{V_{max}\theta_i}{D_c}\right)^{n-2} \ , \tag{B3}$$

where the coefficient α depends upon the functional form of $\Delta\tau/\Delta\tau_{p-r}$; for linear slip-weakening, as for the aging law, $\alpha \sim 0.7$.

[60] Provided the requirement of a small slip-weakening zone is met, equations (B2) and (B3) lead to

$$\frac{\delta(x,t)}{D_c} = A(t)s(\overline{x}) \ , \tag{B4}$$

with

$$A(t) \equiv \left(\ln\frac{V_{max}\theta_i}{D_c}\right)^{n-1} \ ; \quad \overline{x} \equiv \frac{x'}{L_b}\left(\ln\frac{V_{max}\theta_i}{D_c}\right)^{2-n} \ ; \tag{B5}$$

where x' is distance behind the tip, so $0 \le s \le \Pi$ and $0 \le \overline{x} \le \alpha\Pi$. Differentiating (B4),

$$\frac{V}{D_c} = \dot{A}s + A\frac{ds}{d\overline{x}}\frac{d\overline{x}}{dt} \ . \tag{B6}$$

Evaluating this at $V = V_{max}$ and neglecting $\dot{\theta}_i/\theta_i$ in relation to $\dot{V}_{max}/V_{max}$,

$$\begin{aligned} 1 = {} & (n-1)\left(\ln\frac{V_{max}\theta_i}{D_c}\right)^{n-2}\left(\frac{D_c\dot{V}_{max}}{V_{max}^2}\right)s(\overline{x}_m) \\ & + \frac{ds}{d\overline{x}_m}\left[\frac{V_{prop}}{V_{max}}\frac{\mu'}{b\sigma}\left(\ln\frac{V_{max}\theta_i}{D_c}\right) + (2-n)\overline{x}_m\left(\frac{D_c\dot{V}_{max}}{V_{max}^2}\right)\right. \\ & \left.\cdot\left(\ln\frac{V_{max}\theta_i}{D_c}\right)^{n-2}\right] \ , \end{aligned} \tag{B7}$$

where $\overline{x}_m$ denotes the location of $V = V_{max}$ and $ds/d\overline{x}_m$ the slope at that point. The first term in brackets on the right represents the contribution from the translation of a time-invariant slip profile; when this term dominates, equation (54) is recovered ($ds/d\overline{x}_m$ is of order α^{-1}). The first term on the right, equal to zero for the slip law, is due to the increasing amplitude of slip within slip-weakening zone. The second term within brackets, zero for the aging law, comes from the steepening of the slip gradient due to shrinking of the slip-weakening zone. For the slip law simulations of Figure 7, we find empirically that $(D_c\dot{V}_{max}/V_{max}^2)$ is constant and decreases from 0.9 to 0.05 as a/b increases from 0.8 to 0.95. As $\overline{x}_m ds/d\overline{x}_m \sim 0.9$, this term contributes less than 10% of the total for $V_{max}\theta_i/Dc > 10^4$, even for the smaller a/b.

[61] For the aging law, note that because both $\Delta\tau_{p-r}$ and δ_c increase linearly with (V_{max}/V_{bg}), R is time-invariant (equation (49)). For the aging-law simulation of Figure 3, Figure B1b superimposes the stresses near the rightmost tip for the 19 snapshots shown in Figure B1a, scaled to vary from a peak value of 1 at the tip to 0 at the center of the nucleation zone. For $V_{max}/V_{bg} \gtrsim 10^3$–$10^4$ the length of the slip weakening zone asymptotically approaches $\sim 0.75L_b$. Substituting the aging-law fracture energy into (46), the equivalent of equation (47) for the slip profile of the propagating front is

$$\frac{\delta}{D_c} \approx \sqrt{\frac{8}{\pi}}\left(\ln\frac{V_{max}\theta_i}{D_c}\right)\left(\frac{x'}{L_b}\right)^{1/2} \ . \tag{B8}$$

Figure B1e shows δ/D_c divided by $\ln(V_{max}\theta_i/D_c)$ as a function of distance behind the propagating front, for the same 19 snapshots. The solid lines show the right tip, the dashed lines the left (reversed for comparison), and the thick dashed line the estimate $(8/\pi)^{1/2}(x'/L_b)^{1/2}$ from (B8). As suggested by Figure B1b, after about the 4th snapshot the normalized slip asymptotically approaches the same distribution. Outside the slip-weakening region, the dashed line provides a good fit to the slip profiles if it is shifted to intersect the horizontal axis near the center of the slip-weakening region. Within the slip-weakening region, the scaling of the axes shows that the fracture energy requirements are satisfied by increasing the slip amplitude over a fixed length scale, rather than (as for the slip law) by reaching the same slip over an ever-diminishing length scale.

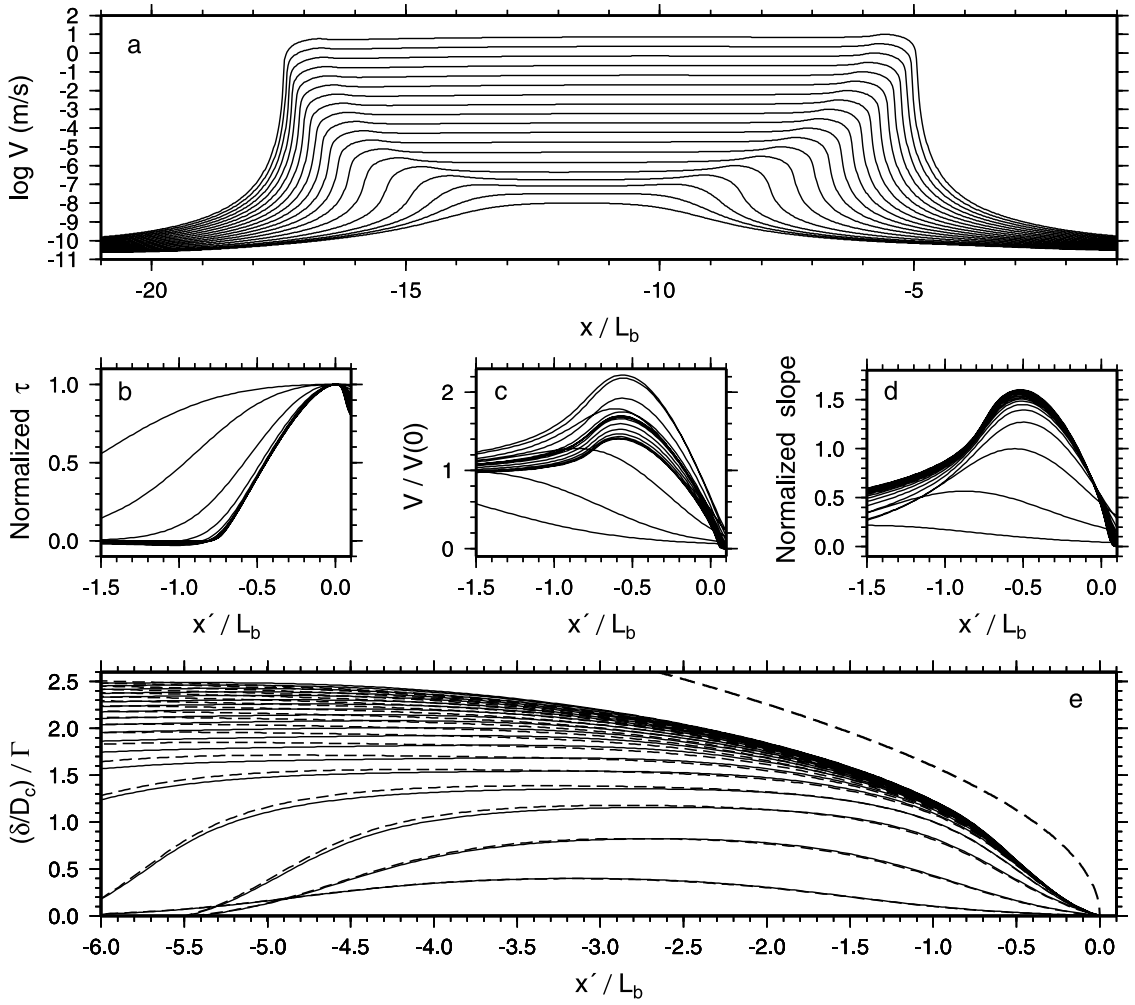

Figure B1. (a), Velocity profiles from Figure 3 with $V_{max} \geq 10^{-8}$ m/s. (b), Shear stress, scaled from a peak value of 1 to zero at the center of the nucleation zone, as a function of normalized distance behind the right tip for all the profiles in Figure B1a. By the fourth profile the slip-weakening region asymptotically approaches $\sim 0.75 L_b$. (c) Slip speed normalized by that at the center of the nucleation zone. (d) Normalized slip gradient $(\delta/D_c)/(x'/L_b)$ for the same profiles, showing the maximum at $\sim 0.5 L_b$ that coincides with the peak slip velocity. (e) Normalized slip, divided by $\Gamma \equiv \ln(V_{max}\theta_i/D_c)$, as a function of distance behind the right (solid) and left (dashed, and reversed for comparison) tips of the nucleation zone. Bold dashed curve indicates the prediction of (B8).

[62] Figures B1c and B1d indicate that for the aging law $\bar{x}_m \sim 0.5$, $s(\bar{x}_m) \sim 0.6$ and $ds/d\bar{x}_m \sim 1.6$. Inserting these values and $n = 2$ into (B7) leads to

$$\frac{V_{prop}}{V_{max}} \approx 0.6\left(1 - 0.6 D_c \frac{\dot{V}_{max}}{V_{max}^2}\right)\frac{\mu'}{b\sigma}\left(\ln\frac{V_{max}\theta_i}{D_c}\right)^{-1}. \qquad \text{(B9)}$$

Noting that the slip speed is quasi-uniform over the interior of the nucleation zone, we might approximate $\dot{V}_{max}/V_{max}^2$ as $\dot{V}/V^2$, so from (33) and (37), (B9) becomes

$$\frac{V_{prop}}{V_{max}} \approx 0.6\left(1 - 0.6\frac{\pi}{2}\frac{b-a}{b}\right)\frac{\mu'}{b\sigma}\left(\ln\frac{V_{max}\theta_i}{D_c}\right)^{-1}. \qquad \text{(B10)}$$

The "1" within the parentheses represents the relative contribution from propagation of a time-invariant slip profile, while the term proportional to $(b-a)/b$ represents the relative contribution from the increasing slip amplitude. The latter approaches zero as a/b approaches 1. Because $0.6\pi/2 \sim 1$, the entire coefficient in parentheses is very nearly a/b.

[63] The ascending curves in Figure B2 show V_{prop} vs. V_{max} for the two ends of the nucleation zone in Figure B1, starting from when the zone begins to expand. Note that the factor of ~ 2 difference in V_{prop} is almost entirely accounted for by a comparable difference in V_{max} behind the fronts, a difference that presumably is controlled by the heterogeneous conditions along the fault. Similar behavior is seen in Figure 9d of Rubin and Ampuero, where the difference between the fronts is closer to an order of magnitude. Note also that the curves in Figure B2 are nearly identical to those of Figure 11 for the slip law, as predicted by the similar coefficients in (B10) and (53). The horizontal curves in

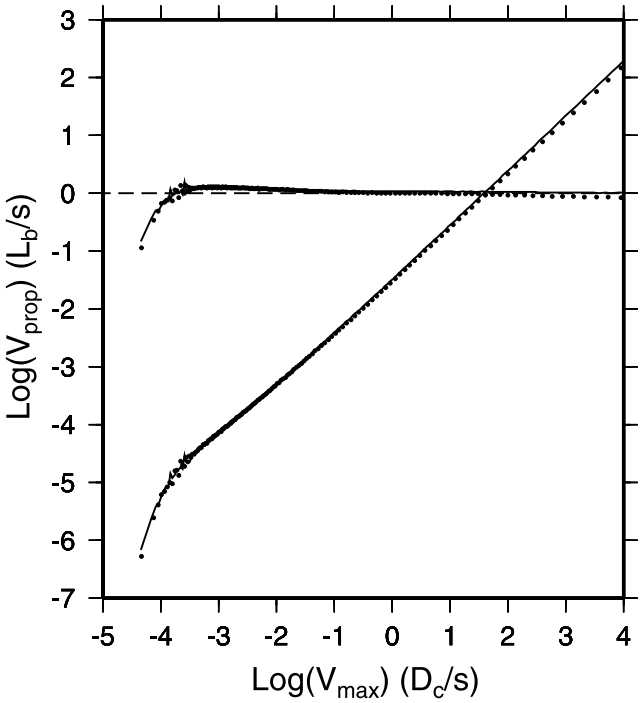

Figure B2. (Ascending curves) Log V_{prop} as a function of log V_{max} for the right (solid) and left (dotted) nucleation fronts in Figure B1. The factor of 2 difference in propagation velocities is explained by a comparable difference in V_{max}. (Horizontal curves) The numerical values of V_{prop} normalized by the prediction of (B10); dashed line indicates a ratio of 1. Equation (B10) is accurate to within a factor of 2 for $V_{max} > 10^{-4}\ D_c/\mathrm{s} = 4 \times 10^{-8}$ m/s, i.e., by the second snapshot in Figure B1.

Figure B2 show V_{prop} normalized by the prediction of (B10); the agreement is quite good.

[64] It should be noted that the aging-law propagation velocity can also be estimated by differentiating the expression for the time-dependent nucleation length. Inserting equations (30) and (31) into (29) leads to

$$L = \frac{L_b}{\pi}\left(\frac{b}{b-a}\right)^2\left[\frac{\ln\frac{V\theta_i}{D_c} - \ln\Omega}{\ln\frac{V}{V_{bg}} - \frac{b}{b-a}\ln\Omega}\right]^2, \qquad \text{(B11)}$$

where V is the quasi-uniform slip speed within the nucleation zone, θ_i is the relatively unperturbed value of θ ahead of the propagating front, and V_{bg} is the hypothetical sliding velocity that at steady state would give rise to the ambient stress (that which would act in the absence of the nucleation displacements). The bracketed term asymptotically approaches 1 in the limit of large V. We find that in our simulations it approaches this value from below, so that L approaches L_∞ from below, but we are unsure how general this result is.

[65] As $\dot{L} = V_{prop}$ for symmetric growth, differentiating (B11) and using (33) and (37) for $\dot{V}/V^2$ leads to

$$\frac{V_{prop}}{V} = \frac{b}{b-a}\left[\ln\left(\frac{D_c}{V_{bg}\theta_i}\right) - \frac{a}{b-a}\ln\Omega\right]\frac{\mu'}{b\sigma}\sqrt{\frac{L}{L_\infty}}\left(\ln\frac{V}{V_{bg}}\right)^{-2}. \qquad \text{(B12)}$$

This expression differs from equation (B10) for V_{prop}/V_{max} by the leading coefficient (including the a/b terms) and an extra $(\ln[V\theta_i/D_c])^{-1}$. To some extent these differences can be accommodated by modest differences between V and V_{max}, as seen in our aging-law simulations. Comparing (B12) and (B10) leads to

$$\frac{V}{V_{max}} \approx 0.6\frac{a}{b}\left(1-\frac{a}{b}\right)\left[\ln\left(\frac{D_c}{V_{bg}\theta_i}\right) - \frac{\pi}{2}\right]^{-1}\sqrt{\frac{L_\infty}{L}}\ln\frac{V}{V_{bg}}, \qquad \text{(B13)}$$

where we have evaluated the relatively insignificant term $a\ln\Omega/(b-a)$ in the limit as a/b approaches 1. The $(1-a/b)$ term shows that, at fixed L/L_∞ and $\ln(V/V_{bg})$, V_{max}/V increases strongly as a/b approaches 1, which qualitatively is consistent with Figures 9a and 10 of *Rubin and Ampuero* [2005a] and other unpublished results in which V_{max}/V increases, during the crack-expansion phase of nucleation, from maximum values of ~1.1 for $a/b = 0.7$, to ~1.5 for $a/b = 0.8$, to ~6 for $a/b = 0.9$, and to ~14 for $a/b = 0.95$.

[66] **Acknowledgments.** Jim Dieterich suggested running the far-below-steady state simulation of Figure 4. We thank Norm Sleep, one anonymous reviewer, and the Associate Editor for helpful reviews. GMT software was used to produce figures. Supported by NSF grants EAR-0126184 and EAR-0538156. JPA is funded by SPICE, an EU Marie Curie Research Training Network. AR gratefully acknowledges a Cox visiting professorship at Stanford University.

References

Bayart, E., A. M. Rubin, and C. Marone (2006), Evolution of fault friction following large velocity jumps, *Eos Trans, AGU*, *87*(52), Fall Meet. Suppl., Abstract S31A-0180.

Beeler, N. M., T. E. Tullis, and J. D. Weeks (1994), The roles of time and displacement in the evolution effect in rock friction, *Geophys. Res. Lett.*, *21*, 1987–1990.

Blanpied, M. L., C. J. Marone, D. A. Lockner, J. D. Byerlee, and D. P. King (1998), Quantitative measure of the variation in fault rheology due to fluid-rock interactions, *J. Geophys. Res.*, *103*, 9691–9712.

Dieterich, J. H. (1992), Earthquake nucleation on faults with rate- and state-dependent friction, *Tectonophysics*, *211*, 115–134.

Dieterich, J. H., and B. D. Kilgore (1994), Direct observation of frictional contacts: New insights for state-dependent properties, *Pure Appl. Geophys.*, *143*, 283–302.

Dieterich, J. H., and B. D. Kilgore (1996), Implications of fault constitutive properties for earthquake prediction, *Proc. Natl. Acad. Sci. USA*, *93*, 3787–3794.

Dragert, H., K. Wang, and T. S. James (2001), A silent slip event on the deeper cascadia subduction interface, *Science*, *292*, 1525–1528.

Freund, L. B. (1979), The mechanics of dynamic shear crack propagation, *J. Geophys. Res.*, *84*, 2199–2209.

Gu, J.-C., J. R. Rice, A. L. Ruina, and S. T. Tse (1984), Slip motion and stability of a single degree of freedom elastic system with rate and state dependent friction, *J. Mech. Phys. Solids*, *32*, 167–196.

Ida, Y. (1973), Maximum acceleration of seismic ground motion, *Bull. Seismol. Soc. Am.*, *63*, 959–968.

Kato, N., and T. E. Tullis (2001), A composite rate- and state-dependent law for rock friction, *Geophys. Res. Lett.*, *28*, 1103–1106.

Kilgore, B. D., M. L. Blanpied, and J. H. Dieterich (1993), Velocity dependent friction of granite over a wide range of conditions, *Geophys. Res. Lett.*, *20*, 903–906.

Lawn, B. (1993), *Fracture of Brittle Solids - 2nd edition*, Cambridge Univ. Press, Cambridge.

Liu, Y., and J. R. Rice (2005), Aseismic slip transients emerge spontaneously in three-dimensional rate and state modeling of subduction earthquake sequences, *J. Geophys. Res.*, *110*, B08307, doi:10.1029/2004JB003424.

Liu, Y., and J. R. Rice (2007), Spontaneous and triggered aseismic deformation transients in a subduction fault model, *J. Geophys. Res.*, *112*, B09404, doi:10.1029/2007JB004930.

Marone, C. (1998), Laboratory-derived friction laws and their application to seismic faulting, *Ann. Rev. Earth Planet. Sci.*, *26*, 643–646.

Nakatani, M. (2001), Conceptual and physical clarification of rate and state friction: Frictional sliding as a thermally activated rheology, *J. Geophys. Res.*, *106*, 13,347–13,380.

Obara, K., and H. Hirose (2006), Non-volcanic deep low-frequency tremors accompanying slow slips in the southwest Japan subduction zone, *Tectonophsyics*, *417*, 33–51.

Perrin, G., J. R. Rice, and G. Zheng (1995), Self-healing slip pulse on a frictional surface, *J. Mech. Phys. Solids*, *43*, 1461–1495.

Ranjith, K., and J. R. Rice (1999), Stability of quasi-static slip in a single degree of freedom elastic system with rate and state dependent friction, *J. Mech. Phys. Sol.*, *47*, 1207–1218.

Rice, J. R. (1980), The mechanics of earthquake rupture, in *Physics of the Earth's Interior, Proc. Int. Sch. Phys. Enrico Fermi*, vol. 78, edited by A. M. Dziewonski and E. Boschi, pp. 555–649.

Rice, J. R. (1993), Spatio-temporal complexity of slip on a fault, *J. Geophys. Res.*, *98*, 9885–9907.

Rice, J. R., N. Lapusta, and K. Ranjith (2001), Rate- and state-dependent friction and the stability of sliding between elastically deformable solids, *J. Mech. Phys. Sol.*, *49*, 1865–1898.

Rubin, A. M., and J.-P. Ampuero (2005a), Earthquake nucleation on (aging) rate and state faults, *J. Geophys. Res.*, *110*, B11312, doi: 10.1029/2005JB003686.

Rubin, A. M., and J.-P. Ampuero (2005b), 3-D earthquake nucleation on rate-and-state faults, *Eos Trans, AGU*, *86*(52), Fall Meet. Suppl., Abstract T13E-07.

Ruina, A. (1983), Slip instability and state variable friction laws, *J. Geophys. Res.*, *88*, 10,359–10,370.

Segall, P., and J. R. Rice (2006), Does shear heating of pore fluid contribute to earthquake nucleation?, *J. Geophys. Res.*, *111*, B11312, doi: 10.1029/2005JB004129.

Sleep, N. H. (2005), Physical basis of evolution laws for rate and state friction, *Geochem. Geophys. Geosyst.*, *6*, Q11008, doi: 10.1029/2005GC000991.

Sleep, N. H. (2006), Real contacts and evolution laws for rate and state friction, *Geochem. Geophys. Geosyst.*, *7*, Q08012, doi: 10.1029/2005GC001187.

J.-P. Ampuero, Institute of Geophysics, Seismology and Geodynamics ETH Honggerberg (HPP), CH-8093 Zurich, Switzerland. (ampuero@erdw.ethz.ch)

A. M. Rubin, Department of Geosciences, Princeton University, Princeton, NJ 08544, USA. (arubin@princeton.edu)